

## Thermal structure and composition of Jupiter's Great Red Spot from high-resolution thermal imaging

Leigh N. Fletcher<sup>a,b,\*</sup>, G.S. Orton<sup>a</sup>, O. Mousis<sup>c,d</sup>, P. Yanamandra-Fisher<sup>a</sup>, P.D. Parrish<sup>a,e</sup>, P.G.J. Irwin<sup>b</sup>, B.M. Fisher<sup>a</sup>, L. Vanzi<sup>f</sup>, T. Fujiyoshi<sup>g</sup>, T. Fuse<sup>g</sup>, A.A. Simon-Miller<sup>h</sup>, E. Edkins<sup>i</sup>, T.L. Hayward<sup>j</sup>, J. De Buizer<sup>k</sup>

<sup>a</sup>Jet Propulsion Laboratory, California Institute of Technology, 4800 Oak Grove Drive, Pasadena, CA 91109, USA

<sup>b</sup>Atmospheric, Oceanic and Planetary Physics, Department of Physics, University of Oxford, Clarendon Laboratory, Parks Road, Oxford OX1 3PU, UK

<sup>c</sup>Institut UTINAM, CNRS-UMR 6213, Observatoire de Besançon, Université de Franche-Comté, Besançon, France

<sup>d</sup>Lunar and Planetary Laboratory, University of Arizona, Tucson, AZ, USA

<sup>e</sup>School of GeoScience, University of Edinburgh, Crew Building, King's Buildings, Edinburgh EH9 3JN, UK

<sup>f</sup>Pontificia Universidad Católica de Chile, Department of Electrical Engineering, Av. Vicuña Mackenna 4860, Santiago, Chile

<sup>g</sup>Subaru Telescope, National Astronomical Observatory of Japan, National Institutes of Natural Sciences, 650 North A'ohoku Place, Hilo, Hawaii 96720, USA

<sup>h</sup>NASA/Goddard Spaceflight Center, Greenbelt, MD 20771, USA

<sup>i</sup>University of California, Santa Barbara, CA 93106, USA

<sup>j</sup>Gemini Observatory, Southern Operations Center, c/o AURA, Casilla 603, La Serena, Chile

<sup>k</sup>SOFIA – USRA, NASA Ames Research Center, Moffett Field, CA 94035, USA

### ARTICLE INFO

#### Article history:

Received 18 June 2009

Revised 18 November 2009

Accepted 4 January 2010

Available online 6 February 2010

#### Keywords:

Jupiter

Atmospheres, Composition

Atmospheres, Structure

### ABSTRACT

Thermal-IR imaging from space-borne and ground-based observatories was used to investigate the temperature, composition and aerosol structure of Jupiter's Great Red Spot (GRS) and its temporal variability between 1995 and 2008. An elliptical warm core, extending over 8° of longitude and 3° of latitude, was observed within the cold anticyclonic vortex at 21°S. The warm airmass is co-located with the deepest red coloration of the GRS interior. The maximum contrast between the core and the coldest regions of the GRS was 3.0–3.5 K in the north–south direction at 400 mbar atmospheric pressure, although the warmer temperatures are present throughout the 150–500 mbar range. The resulting thermal gradients cause counter-rotating flow in the GRS center to decay with altitude into the lower stratosphere. The elliptical warm airmass was too small to be observed in IRTF imaging prior to 2006, but was present throughout the 2006–2008 period in VLT, Subaru and Gemini imaging.

Spatially-resolved maps of mid-IR tropospheric aerosol opacity revealed a well-defined lane of depleted aerosols around the GRS periphery, and a correlation with visibly-dark jovian clouds and bright 4.8- $\mu\text{m}$  emission. Ammonia showed a similar but broader ring of depletion encircling the GRS. This narrow lane of subsidence keeps red aerosols physically separate from white aerosols external to the GRS. The visibility of the 4.8- $\mu\text{m}$  bright periphery varies with the mid-IR aerosol opacity of the upper troposphere. Compositional maps of ammonia, phosphine and para-H<sub>2</sub> within the GRS interior all exhibit north–south asymmetries, with evidence for higher concentrations north of the warm central core and the strongest depletions in a symmetric arc near the southern periphery. Small-scale enhancements in temperature, NH<sub>3</sub> and aerosol opacity associated with localized convection are observed within the generally-warm and aerosol-free South Equatorial Belt (SEB) northwest of the GRS. The extent of 4.8- $\mu\text{m}$  emission from the SEB varied as a part of the 2007 'global upheaval,' though changes during this period were restricted to pressures greater than 500 mbar. Finally, a region of enhanced temperatures extended southwest of the GRS during the survey, restricted to the 100–400 mbar range and with no counterpart in visible imaging or compositional mapping. The warm airmass was perturbed by frequent encounters with the cold airmass of Oval BA, but no internal thermal or compositional effects were noted in either vortex during the close encounters.

© 2010 Elsevier Inc. All rights reserved.

### 1. Introduction

Of all the meteorological features in our Solar System, Jupiter's Great Red Spot (GRS) is perhaps the best known and most often observed. Jupiter's largest anticyclonic vortex serves as a paradigm

\* Corresponding author. Address: Atmospheric, Oceanic and Planetary Physics, Department of Physics, University of Oxford, Clarendon Laboratory, Parks Road, Oxford OX1 3PU, UK.

E-mail address: [fletcher@atm.ox.ac.uk](mailto:fletcher@atm.ox.ac.uk) (L.N. Fletcher).

for the study of the formation and dynamics of large storms on gas giants, and infrared imaging of the storm system and its surrounding atmosphere can yield a wealth of information about the three-dimensional structure and composition. This paper uses ground-based thermal-IR imaging and spectroscopy to investigate two aspects of the GRS and its turbulent environs. Firstly, we search for *evidence of small-scale thermal inhomogeneities within and surrounding the vortex*, and correlate these with structures observed at visible wavelengths to study vertical motions and aerosols associated with the GRS. We utilize the high spatial resolutions offered by observatories with 8-m primary mirrors (namely the ESO Very Large Telescope, Subaru Telescope and Gemini South Observatory), in some cases equaling and surpassing the infrared spatial resolutions provided by Galileo and Cassini. Secondly, we investigate *long-term changes in these properties using thermal-IR imaging acquired between 1995 and 2008*, to provide a context for observations from visiting spacecraft. These investigations were motivated by (a) the disparity between the spatial resolutions at visible and thermal-IR wavelengths compared in previous studies; and (b) the need to understand long-term variability of the thermal field to better constrain dynamical modeling of jovian vortices.

### 1.1. Great Red Spot from visible imaging

Visible imaging and cloud-tracking from spacecraft has significantly enhanced our understanding of atmospheric motion within the GRS. Approximately  $22,000 \times 11,000$  km in size (from 1996 observations, Vasavada et al., 1998), the GRS is distinguished from smaller white ovals by its high-velocity annular collar which surrounds a quiescent interior (Mitchell et al., 1981). Most of the velocity and vorticity of the GRS is located in a thin anticyclonic ring at 70–85% of the radius (Sada et al., 1996; Simon-Miller et al., 2002) where circulation takes approximately 5 days. The GRS sits in a broad axisymmetric region centered at the peak of Jupiter's fastest retrograde (westward) jet at  $17.5^\circ\text{S}$  planetocentric latitude (hereafter all latitudes are quoted as planetocentric) which is deflected north around the GRS periphery (Limaye, 1986; Porco et al., 2003). The jet separates the warm, cyclonic South Equatorial Belt (SEB) from the cool, anticyclonic South Tropical Zone (STrZ). The SEB is almost entirely 'pinched-off' at its northern edge by the GRS (Rogers, 1995), and a great amount of activity and turbulence is apparent to the northwest of the vortex, characterized by short-lived bursts of fresh bright clouds plus spectroscopic detections of  $\text{NH}_3$  ice and lightning (indicative of moist convection and rapid updrafts, Baines et al., 2002; Vasavada and Showman, 2005). A prograde (eastward) jet at  $23.8^\circ\text{S}$  is deflected around the southern periphery of the GRS, to the south of which lies the southern temperate region, consisting of the warm and visibly-dark South Temperate Belt (STB) and the ephemeral bright South Temperate Zone (STZ).

### 1.2. Previous thermal characterization of the GRS

In the thermal-IR, low spatial-resolution temperature maps from Voyager (Infrared Radiometer and Spectrometer, IRIS, Hanel et al., 1977), Galileo (Photopolarimeter–Radiometer, PPR, Russell et al., 1992) and Cassini (Composite Infrared Spectrometer, CIRS, Flasar et al., 2004) identified the GRS as a cold-core feature (Hanel et al., 1979; Flasar et al., 1981; Orton et al., 1996; Sada et al., 1996; Simon-Miller et al., 2002) surrounded by a warm annulus, consistent with centralized upwelling and subsidence at the edges of an anticyclonic vortex. This was consistent with cloud-clearing at the edges inferred from the ring of bright  $5\text{-}\mu\text{m}$  emission surrounding the vortex (Terrile et al., 1979), and is associated with a peripheral ring of cyclonic vorticity (Choi et al., 2007). Thermal wind cross-sections derived from Voyager data implied a despinning of the anticyclonic motion with altitude into the lower stratosphere (Fla-

sar et al., 1981). Galileo/PPR measurements, though limited by Galileo's low telemetry rate and spectral coverage due to problems associated with the filter wheel, were used to show the presence of a warm periphery to the south of the GRS within a dark visible ring, and that the warmest temperatures occurred in visibly-dark regions of the SEB (Orton et al., 1996). However, none of these thermal imaging datasets have been able to provide spatial resolutions close to visible observations for direct comparison.

Compositional maps derived from thermal-IR spectroscopy have generally been consistent with strong upwelling motion over the GRS core. Voyager/IRIS first demonstrated that the GRS exhibits a local minimum in para- $\text{H}_2$ , indicative of vertical advection at rates faster than the equilibration timescale for ortho-para  $\text{H}_2$  (Sada et al., 1996; Simon-Miller et al., 2002). Aerosol opacities derived from 5- and  $44\text{-}\mu\text{m}$  Voyager/IRIS observations (Sada et al., 1996) showed local maxima over the GRS, but the spatial distribution of  $\text{NH}_3$  gas (Griffith et al., 1992; Sada et al., 1996; Lara et al., 1998; Achterberg et al., 2006) is less certain, with Griffith et al. (1992) observing a localized  $\text{NH}_3$  depletion above 350 mbar, and others finding a local maximum over the GRS. Similar uncertainties are found in the spatial distribution of  $\text{PH}_3$ , with Cassini/CIRS results showing localized enhancements (Irwin et al., 2004), whereas both Voyager/IRIS spectra in 1981 (Griffith et al., 1992) and IRTF spectroscopy in 1991 (Lara et al., 1998) indicated no  $\text{PH}_3$  variations across the GRS region. The reproducibility of the spatial distributions of aerosols and gaseous composition will be tested in Section 3, and high-resolution maps of temperatures, tropospheric aerosol opacity, ammonia and para- $\text{H}_2$  will be derived from ground-based thermal imaging.

### 1.3. Previous temporal variability studies

In Section 4 we investigate the temporal variability of the thermal characteristics of the GRS for comparison with visible results. Although ground-based observations of the GRS at visible wavelengths suggest that the storm has persisted since at least 1831 (Rogers, 1995), temporal variations in the visible appearance of the GRS and its surroundings have been recorded. Firstly, it drifts in longitude with respect to a uniformly rotating coordinate system (Rogers, 1995; Beebe, 1994), accelerated and decelerated by passing disturbances or changes to the SEB. Secondly, small variations in the central latitude ( $\pm 0.5^\circ$ ) may alter the interaction of the vortex with the surrounding windfield (Rogers, 1995). Furthermore, the east-west extent of the vortex shrunk with time by  $8 \pm 3^\circ$  longitude from 1979 to 2000 (Simon-Miller et al., 2002), leading to a 15% reduction in the area enclosed by the high-velocity collar between 1996 and 2006 (Asay-Davis et al., 2009). Visible imaging demonstrated that central parts of the vortex were chaotic in nature (Mitchell et al., 1981; Sada et al., 1996; Vasavada et al., 1998), with possible indications of counter-rotating flow (Vasavada et al., 1998; Choi et al., 2007). Small-scale cyclonic vortices and organized eddy motion were present during the Voyager epoch (Sada et al., 1996), absent during 1996 Galileo observations (Vasavada et al., 1998) and possibly present again in 2000 (Simon-Miller et al., 2002). Small-scale structures and bright convective cloud features that appear in the turbulent region northwest of the GRS are transient in nature (Reuter et al., 2007; Baines et al., 2007), and the GRS undergoes frequent close passages, mergers and interactions with smaller storms caught up in the zonal flow. The thermal effects of some of these temporal variations will be investigated in Section 4. A full review of the dynamics, stability and behavior of jovian vortices can be found in Vasavada and Showman (2005).

## 2. Observations

The study of the GRS and its environs over a long temporal baseline requires analysis of thermal imaging data from a wide variety

of sources (Table 1). Although sophisticated spacecraft (Voyager, Galileo, Cassini and New Horizons) have visited Jupiter during the past several decades, their glimpses of the GRS offer only occa-

sional snapshots sparsely separated in time. This is particularly true for the temporal and spatial coverage in the thermal infrared, from which temperature structure and gaseous composition can be

**Table 1**

Summary of datasets used in this study, with a reference to the figure where a particular dataset was used. Note that dates which were considered but ultimately discarded from the figures (as they did not add anything to the discussion) are available upon request from the author. ID numbers are given for the awarded time on Subaru and VLT.

Source	Date	Figure	Comments
Galileo/PPR	1996-06-26	Not shown	G1; images in all five filters, low resolution
Galileo/PPR	1996-06-27	Not shown	G1; images in all five filters, poor spatial coverage
Galileo/PPR	1997-04-04	3	G7; image at 35.5 $\mu\text{m}$ only
Galileo/PPR	2000-12-29	3	G29; only two filters (16.8, 21.0 $\mu\text{m}$ ), high resolution
Hubble WFPC2	1997-04-04	3	Cycle 6; Prop 6452; PI: A.A. Simon-Miller
Hubble ACS	2006-04-24	1, 6	Prop ID 10782; PI: I. de Pater
Hubble WFPC2	2008-05-15	2, 6	Prop ID 11498; PI: A.A. Simon-Miller
Cassini/CIRS	2000-12-31	4	8500 spectra in ATMOS02A map, 77°N to 79°S
Cassini/ISS NAC	2000-12-12	3 and 4	Combined 451 and 750 nm image PIA07782
VLT/VISIR	2006-04-09	6 and 5	Prog. ID: 276.C-5055
VLT/VISIR	2006-04-10	10	Prog. ID: 276.C-5055
VLT/VISIR	2007-03-01	6	Prog. ID: 278.C-5023
VLT/VISIR	2007-08-15	6	Prog. ID: 279.C-5043
VLT/VISIR	2008-05-18	6	Prog. ID: 381.C-0134
VLT/VISIR	2008-07-04	7	Prog. ID: 081.C-0137
VLT/VISIR	2008-08-10	7	Prog. ID: 081.C-0141
VLT/VISIR	2008-09-03	7	Prog. ID: 081.C-0137
Subaru/COMICS	2008-06-24	Not shown	Prog. ID: S07B-015, features too close to limb
Subaru/COMICS	2008-09-14	7–9	Prog. ID: S08B-031
Subaru/COMICS	2008-09-15	Not shown	Prog. ID: S08B-031; identical to 2008-09-14
Gemini/TReCS	2007-02-12	13	Prog. ID: GS-2007A-Q39
IRTF/MIRLIN	1995-07-06	11	Prog. ID: 049
IRTF/MIRLIN	1996-06-01	11	Prog. ID: 028
IRTF/MIRLIN	1997-11-07	11	Prog. ID: 030
IRTF/MIRLIN	1998-01-21	Not shown	Prog. ID: 062
IRTF/MIRLIN	1998-07-20	Not shown	Prog. ID: 040
IRTF/MIRLIN	1998-09-28	11	Prog. ID: 005
IRTF/MIRLIN	1999-07-02	Not shown	Prog. ID: 004
IRTF/MIRLIN	1999-08-13	Not shown	Prog. ID: 039
IRTF/MIRLIN	1999-10-08	11	Prog. ID: 039
IRTF/MIRLIN	2000-02-22	Not shown	Prog. ID: 009
IRTF/MIRLIN	2000-06-10	Not shown	Prog. ID: 009
IRTF/MIRLIN	2000-10-04	11	Prog. ID: 009
IRTF/MIRLIN	2000-12-29	Not shown	Prog. ID: 009
IRTF/MIRLIN	2000-12-30	11	Prog. ID: 009
IRTF/MIRLIN	2001-03-06	11	Prog. ID: 007
IRTF/MIRLIN	2001-03-07	Not shown	Prog. ID: 007
IRTF/MIRLIN	2001-05-01	Not shown	Prog. ID: 007
IRTF/MIRLIN	2001-05-03	Not shown	Prog. ID: 007
IRTF/MIRLIN	2001-10-23	Not shown	Prog. ID: 021
IRTF/MIRLIN	2002-02-07	11	Prog. ID: 031
IRTF/MIRLIN	2002-02-08	11	Prog. ID: 031
IRTF/MIRLIN	2003-02-25	11	Prog. ID: 027
IRTF/MIRLIN	2003-02-27	Not shown	Prog. ID: 027
IRTF/MIRSI	2004-03-26	11	Prog. ID: 997
IRTF/MIRSI	2005-01-31	Not shown	Prog. ID: 038
IRTF/MIRSI	2005-05-06	11	Prog. ID: 004
IRTF/MIRSI	2005-06-14	Not shown	Prog. ID: 004
IRTF/MIRSI	2006-01-29	11	Prog. ID: 006
IRTF/MIRSI	2006-01-30	Not shown	Prog. ID: 006
IRTF/MIRSI	2006-04-16	11	Prog. ID: 006
IRTF/MIRSI	2006-06-20	11	Prog. ID: 006
IRTF/MIRSI	2006-07-05	11	Prog. ID: 996
IRTF/MIRSI	2006-07-10	11	Prog. ID: 996
IRTF/MIRSI	2007-03-18	11	Prog. ID: 020
IRTF/MIRSI	2007-05-30	11	Prog. ID: 020
IRTF/NSFCAM	1999-01-05	Not shown	Prog. ID: 999
IRTF/NSFCAM	1999-02-08	Not shown	Prog. ID: 999
IRTF/NSFCAM	1999-02-15	Not shown	Prog. ID: 049
IRTF/NSFCAM	1999-05-24	Not shown	Prog. ID: 999
IRTF/NSFCAM	1999-06-29	Not shown	Prog. ID: 004
IRTF/NSFCAM	1999-07-08	Not shown	Prog. ID: 049
IRTF/NSFCAM	1999-07-18	12	Prog. ID: 036
IRTF/NSFCAM	1999-07-28	Not shown	Prog. ID: 049
IRTF/NSFCAM	1999-08-11	Not shown	Prog. ID: 039
IRTF/NSFCAM	1999-08-12	Not shown	Prog. ID: 039

Table 1 (continued)

Source	Date	Figure	Comments
IRTF/NSFCAM	1999-08-23	Not shown	Prog. ID: 076
IRTF/NSFCAM	1999-09-14	Not shown	Prog. ID: 039
IRTF/NSFCAM	1999-10-10	Not shown	Prog. ID: 039
IRTF/NSFCAM	1999-10-16	Not shown	Prog. ID: 073
IRTF/NSFCAM	1999-11-25	12	Prog. ID: 039
IRTF/NSFCAM	1999-11-26	Not shown	Prog. ID: 039
IRTF/NSFCAM	2000-02-07	12	Prog. ID: 050
IRTF/NSFCAM	2000-02-11	Not shown	Prog. ID: 003
IRTF/NSFCAM	2000-03-02	Not shown	Prog. ID: 006
IRTF/NSFCAM	2000-04-12	Not shown	Prog. ID: 043
IRTF/NSFCAM	2000-08-12	Not shown	Prog. ID: 010
IRTF/NSFCAM	2000-08-19	Not shown	Prog. ID: 010
IRTF/NSFCAM	2000-09-23	Not shown	Prog. ID: 010
IRTF/NSFCAM	2000-09-27	Not shown	Prog. ID: 010
IRTF/NSFCAM	2000-10-05	Not shown	Prog. ID: 009
IRTF/NSFCAM	2000-11-11	Not shown	Prog. ID: 010
IRTF/NSFCAM	2000-12-24	Not shown	Prog. ID: 010
IRTF/NSFCAM	2000-12-29	Not shown	Prog. ID: 009
IRTF/NSFCAM	2000-12-30	12	Prog. ID: 009
IRTF/NSFCAM	2001-01-08	Not shown	Prog. ID: 010
IRTF/NSFCAM	2001-01-19	12	Prog. ID: 010
IRTF/NSFCAM	2001-03-07	Not shown	Prog. ID: 007
IRTF/NSFCAM	2002-01-11	Not shown	Prog. ID: 001
IRTF/NSFCAM	2002-02-07	Not shown	Prog. ID: 031
IRTF/NSFCAM	2002-02-08	Not shown	Prog. ID: 031
IRTF/NSFCAM	2002-02-11	12	Prog. ID: 031
IRTF/NSFCAM	2002-03-14	12	Prog. ID: 050
IRTF/NSFCAM	2003-02-23	12	Prog. ID: 027
IRTF/NSFCAM	2003-12-18	12	Prog. ID: 995
IRTF/NSFCAM	2004-02-08	Not shown	Prog. ID: 042
IRTF/NSFCAM	2004-02-09	12	Prog. ID: 042
IRTF/NSFCAM2	2006-04-16	6	Prog. ID: 006
IRTF/NSFCAM2	2006-04-25	12	Prog. ID: 999
IRTF/NSFCAM2	2006-05-25	12	Prog. ID: 006
IRTF/NSFCAM2	2006-06-26	12	Prog. ID: 006
IRTF/NSFCAM2	2007-02-24	12, 6	Prog. ID: 020
IRTF/NSFCAM2	2007-03-18	12	Prog. ID: 020
IRTF/NSFCAM2	2007-05-30	12	Prog. ID: 020
IRTF/NSFCAM2	2008-06-16	12	Prog. ID: 062
IRTF/NSFCAM2	2008-07-10	12, 7	Prog. ID: 062
IRTF/NSFCAM2	2008-07-11	Not shown	Prog. ID: 062
IRTF/NSFCAM2	2008-08-07	12, 7	Prog. ID: 002
IRTF/NSFCAM2	2008-09-24	12, 7	Prog. ID: 993

determined. The datasets included in this work are outlined in the following paragraphs, describing incremental increases in spatial resolution (and hence in our understanding of small-scale thermal structures associated with the GRS) from NASA/IRTF, Galileo/PPR, Cassini/CIRS and 8.2-m ground-based observatories.

### 2.1. NASA/IRTF observations

NASA's Infrared Telescope Facility (IRTF) provided support for the Galileo, Cassini and New Horizons observations of Jupiter, acquiring imaging in the near-IR with NSFCAM and NSFCAM2 and in the mid-IR with the MIRLIN (Ressler et al., 1994) and MIRSI (Deutsch et al., 2003) cameras. Diffraction-limited spatial resolutions with a 3-m telescope of 1230 km ( $1.0^\circ$ ), 1970 km ( $1.6^\circ$ ) and 6260 km ( $5.0^\circ$ ) are possible at 4.8, 7.70 and 24.50  $\mu\text{m}$ , respectively. Table 1 provides the dates of all of the GRS observations considered in this study. MIRSI and MIRLIN mid-IR images were reduced, geometrically registered, and radiometrically calibrated following the methods described by Fletcher et al. (2009b). As pointed out by Fletcher et al. (2009b), absolute calibration via scaling to match the Cassini/CIRS observations (described below) provides a self-consistent dataset for comparison over long baseline. Although large-scale variations in global brightness will not be accounted for, this technique permits the study of thermal variations on small

er scales. NSFCAM and NSFCAM2 images were reduced, coadded, geometrically registered and mapped using the same reduction software. The diffraction-limited spatial resolution offered by the 3-m primary mirror is insufficient to resolve the internal details of the GRS, but IRTF observations provide a self-consistent temporal record of the GRS evolution.

### 2.2. Galileo/PPR observations

The Galileo spacecraft spent 8 years in orbit around Jupiter from December 1995 until September 2003, carrying with it the Photopolarimeter–Radiometer (PPR) that mapped the jovian troposphere using five filters centered at 16.8, 21.0, 27.5, 35.5 and 45–100  $\mu\text{m}$  (Russell et al., 1992). However, spatial coverage was ultimately limited by Galileo's low telemetry rates, and spectral coverage was restricted to only one or two channels by problems with the filter wheel after the first orbit. The only published example of GRS observations from PPR (June 26th 1996) was given in Orton et al. (1996), which featured a 2800-km spatial resolution ( $2.2^\circ$ ) that far surpassed ground-based observatories with 3-m primary mirrors at the same wavelengths. However, their Fig. 2 showed thermal maps quite unlike those observed from the ground, and a lack of coherent structure within the GRS itself. We present two further observations on April 4th 1997 and

December 29th 2000, the latter being concurrent with the Cassini flyby of Jupiter (see below) and having a higher spatial resolution (as good as 1200 km). Each set of PPR images is compared to a visible image (described in the caption to Fig. 3) in order to compare the visible and thermal appearance of the GRS at a similar epoch.

### 2.3. Cassini/CIRS observations

Cassini flew by Jupiter in December 2000, enroute to Saturn. Near closest approach, the Cassini Composite Infrared Spectrometer (CIRS, a dual Fourier transform spectrometer, Flasar et al., 2004) was capable of achieving spatial resolutions of 2–3° latitude in the equatorial region (2500–3700 km) using 600–1400 cm<sup>-1</sup> spectra with a 2.5-cm<sup>-1</sup> resolution. As described in Section 1, CIRS observations of the GRS have been previously analyzed by Simon-Miller et al. (2002), Irwin et al. (2004) and Achterberg et al. (2006). However, several improvements have been made to the CIRS calibration method, including the reduction of electrical interference patterns and spectral ripples from apodization, and the increased number of deep space reference spectra used to calibrate the data, increasing the signal-to-noise level for each individual spectrum. We coadd spectra from the ATMOS2A map (December 31st 2000, Table 1) in bins 2° latitude and 4° longitude in size (slightly smaller than the gridding used by Achterberg et al. (2006) and Irwin et al. (2004), because of the increased signal-to-noise in the recalibrated data), stepped to achieve Nyquist sampling of the dataset. Furthermore, we employ the updated retrieval methods described by Fletcher et al. (2009a) to (a) improve on the PH<sub>3</sub> determinations of Irwin et al. (2004), and (b) produce the first map of mid-IR aerosol opacity over the GRS from CIRS observations.

### 2.4. Eight-meter telescope facilities

To probe the small-scale structures associated with the GRS, we initiated a campaign of thermal-IR observations of Jupiter between April 9th 2006 and September 14th 2008 using Subaru/COMICS (Cooled Mid-IR Camera and Spectrograph on the Subaru telescope of Japan, Kataza et al., 2000), VLT/VISIR (mid-IR imager and spectrometer on the ESO Very Large Telescope, Rio et al., 1998) and Gemini/TReCS (Thermal-Region Camera Spectrograph on Gemini-South, De Buizer et al., 2005). During this time span, VISIR observed Jupiter's southern hemisphere on eight occasions to capture the evolution of the GRS. COMICS observed the GRS three times in 2008 (June 24th, September 14th and 15th), and TReCS observed the GRS once on February 12th 2007. Diffraction-limited imaging at 8.2-m telescopes provided spatial resolutions of 720 km (0.6°), 1600 km (1.3°) and 2300 km (1.8°) at 7.70, 17.20 and 24.50 μm, respectively, surpassing the resolution of Cassini/CIRS and almost rivaling the highest-resolution maps from the Galileo PPR. This dataset has the advantage over Galileo/PPR in the wide spatial and spectral coverage, coupled with the multiple opportunities offered by ground-based observing.

COMICS, VISIR and TReCS data were reduced, geometrically registered, cylindrically projected and absolutely calibrated using the techniques described by Fletcher et al. (2009b). In addition, because the diffraction-limited spatial resolution worsens at longer wavelengths, the PIXON image reconstruction technique of Puetter et al. (1999) (tested and implemented in Fletcher et al. (2009b)) was used to deconvolve the point spread function (PSF) from the data and reduce the random noise on the images. Images of a star in each filter were modeled to estimate the PSF, carefully checking each reconstructed target-image for the occurrence of artifacts. The random noise was visibly reduced, allowing tighter constraints on the retrieved temperature and composition in the retrieval process, described below.

### 2.5. Atmospheric retrievals

Fletcher et al. (2009b) described the use of an optimal estimation retrieval algorithm, Nemesis (Irwin et al., 2008), to derive Jupiter's atmospheric temperature, aerosol opacity and ammonia gas distribution from filtered thermal-IR imaging between 7 and 25 μm. Provided that sufficient Q-band observations (17–25 μm) were acquired to constrain the vertical temperature structure in the 100–600 mbar range, this technique permits the extraction of the NH<sub>3</sub> abundance in the 400–700 mbar range and aerosol haze opacities in the 200–500 mbar range from the *relative* brightness variations in N-band (7–13 μm) filtered imaging. This is the case for Jupiter observations from VISIR (six filters were regularly acquired, 8.59, 10.77, 13.04, 17.65, 18.72 and 19.50 μm) and from COMICS (8.70, 10.30, 17.65, 18.75, 20.50, 24.50 μm), but not from TReCS (which has only a single temperature-sensitive filter at 18.3 μm). The absence of full  $T(p)$  retrieval capabilities from TReCS would make compositional retrievals unreliable, so they are not considered here. Furthermore, the presence of the additional Q-filter on COMICS at 24.5 μm allows us to derive the para-hydrogen fraction,  $f_p(p)$ , by defining the spectral shape of the continuum associated with the  $S(0)$  and  $S(1)$  transitions, something only previously obtained from Voyager/IRIS (Sada et al., 1996; Simon-Miller et al., 2002).

Finally, we include a reanalysis of the Cassini/CIRS ATMOS2A from December 31st 2000. This was motivated by (a) the need to demonstrate consistency between aerosol morphologies retrieved from full spectroscopy and filtered imaging (see Section 3.4); (b) the application of the simultaneous retrieval techniques for the phosphine and aerosol distribution described by Fletcher et al. (2009a); and (c) the recalibration of the CIRS dataset to improve the noise qualities of individual spectra. The retrieved temperature, aerosol opacity and NH<sub>3</sub> maps will be compared directly to retrievals from ground-based data (see Section 3). The reference atmospheric structure and sources of spectral linedata for both CIRS and ground-based retrievals are described in full by Fletcher et al. (2009a).

## 3. Results I: the structure of the Great Red Spot

This section presents high spatial resolution maps of retrieved atmospheric parameters, with the goal of identifying previously unresolved thermal and compositional variations. The aim is to use such variations as constraints on atmospheric motion in the regions within and surrounding the GRS.

### 3.1. Inhomogeneous structure within the GRS core

VISIR imaging in April 2006 (Fig. 1) was the first to demonstrate the presence of a coherent warm region centered within the cold anticyclonic vortex at 21°S. This inhomogeneity in the core region was warmer than the surrounding cold vortex in all filters except 8.59 μm, implying that the feature is present over a range of altitudes from 80 to 600 mbar (the 17.65-μm filter probes the tropopause temperatures, whereas the 13.04-μm filter senses temperature contrasts at depth). The warm region is typically located 1–2° south of the geometric center of the elliptical GRS. The warm GRS center was identifiable on all additional observation dates between 2006 and 2008 (VISIR, COMICS and TReCS), though the spatial morphology was affected by variable seeing conditions on the different dates. The 8.59-μm filter in Fig. 1, which is the most sensitive to tropospheric aerosol opacity, demonstrates lower brightness in the core region compared to the other filters, with an arc of brighter emission extending from west to east around the core. Based on the highest-resolution

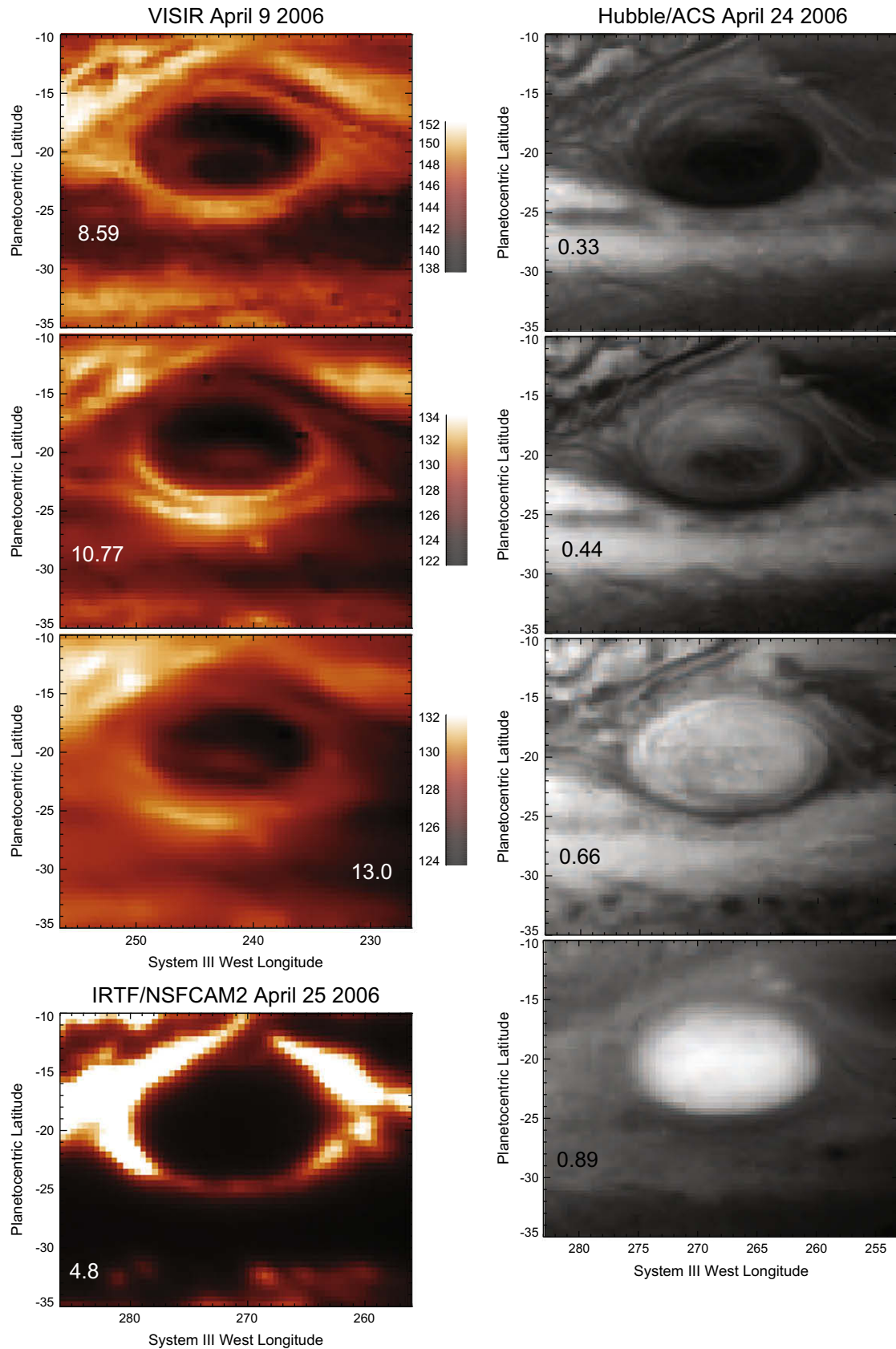


**Fig. 1.** Correlation between thermal imaging from VLT/VISIR (April 9th 2006), visible imaging from Hubble/ACS (April 24th 2006) and 4.8- $\mu\text{m}$  imaging from IRTF/NSFCAM2. The wavelength of each filter (in  $\mu\text{m}$ ) is given within each separate panel. The high spatial resolutions offered by VLT/VISIR observations indicates a central warm core interior to the GRS, which is also present in Q-band filters (not shown). The warm core corresponds to the darkest regions (i.e. most-absorbing) in the shortest Hubble/ACS wavelengths.

filter (8.59  $\mu\text{m}$ ), and assuming that the warm temperatures at longer wavelengths are co-located precisely with the structures seen here, we estimate the size of the elliptical warm core to be  $8^\circ$  longitude and  $3^\circ$  latitude (approximately 9000 by 3700 km), comprising 18% of the internal area of the GRS, as measured from the 8.59- $\mu\text{m}$  image.

No comparable structures were observed within the GRS at 4.8  $\mu\text{m}$  (NSFCAM2 on April 25th, 16 days later, bottom left of Fig. 1), even when the filtered images were stretched in contrast. Because darker regions of 4.8- $\mu\text{m}$  images are interpreted as high aerosol opacity that attenuates radiances from deeper atmospheric levels (2–4 bars, Flasar et al., 1981), this implies that the features seen in mid-IR images are located above the main source of 4.8- $\mu\text{m}$  opacity in the GRS.

The high thermal-IR spatial resolution of the VISIR data permits direct comparison with Hubble Advanced Camera for Surveys (ACS) imaging from 15 days later (right-hand panels in Fig. 1). Although atmospheric circulation within the vortex will have redistributed individual cloud-tracers between the thermal and visible observations, a large coherent structure is still visible in the center of the HST images. This correlation was also present in 2008 (Fig. 2), when VISIR data on May 18th 2008 was separated from Hubble Wide-Field Planetary Camera 2 (WFPC2) imaging by only 3 days. Correlation analyses on both dates indicated that the location of the warm core corresponded with the lowest reflectivity in short-wavelength filters (this was evident at 260, 340, 390, 410, 440, and 470 nm) and with the highest reflectivity at 890 nm. Regions with cooler temperatures, surrounding the warm core, were slightly less absorbing in the blue, so we conclude that the warmest locations of the GRS interior correspond with the deepest red (blue-absorbing) coloration of the GRS clouds. This suggests a dynamical or chemical link between the red coloration and the temperature field. If the warm temperatures are due to weak atmospheric subsidence in the GRS core, the deep red clouds could be at higher pressures than the surrounding pale regions. Alternatively, the warm temperatures could alter the chemistry, or lead to sublimation of material from aerosols, revealing the red coloration. Dynamical and chemical modeling are required to reveal the underlying cause of this correlation between cloud coloration and the temperature field.

### 3.2. Absence from spacecraft observations

It is reasonable to ask why such a large feature was not observed in thermal observations by visiting spacecraft. For Galileo, the issue was spatial coverage rather than spatial resolution. Fig. 3 shows brightness temperatures derived from Galileo/PPR in April 1997 and December 2000, compared to visible images taken at similar times. The 1997 filter (35.5  $\mu\text{m}$ ) shows no evidence for coherent internal structures, and an oscillating southern periphery which had no counterpart in visible images. The December 2000 data provided higher spatial resolutions, but the core of the GRS was barely covered in the imaging, and showed the usual decrease in temperatures towards the GRS center at  $20^\circ\text{S}$ . In the case of Cassini, the  $3^\circ$  latitudinal extent of the warm core was similar to the spatial resolution of the ATMOS2A map. Furthermore, the signal-to-noise in individual spectra would have been insufficient to detect the perturbation to the thermal field. The thermal maps and temperature cross-sections in Fig. 4, updated from the work of Simon-Miller et al. (2002) to include a full derivation of mid-IR aerosol opacity and composition (see below), do not show any evidence for the warm center, despite the presence of the deep red GRS core in the accompanying Cassini/ISS imaging.

### 3.3. Temperatures and winds

The presence of the warm core has implications for atmospheric motion within the GRS interior. Fig. 5 shows an example of the retrieved temperature structure for the first date in the VISIR observation sequence (April 9th, 2006). The top panels show temperature maps at two different pressure levels, the center panels show north–south and east–west cross-sections through the thermal retrievals, subtracted from the mean temperatures of the atmosphere surrounding the GRS. Solid lines show temperatures cooler than the surroundings, whereas dotted lines show warmer temperatures. These plots indicate that the warm core, located at  $20^\circ\text{S}$ ,  $242^\circ\text{W}$  on this date, is present for pressures between 150 and 500 mbar. At lower pressures, the GRS center is the coldest region of the vortex. At pressures greater than 500–600 mbar, the contours begin to level out, but this may simply be a result of the smoothing assumptions implicit in the retrieval process (see, e.g. cite09fletcherimaging). As the warm central core was identified in all of the VISIR filters, we cannot constrain the maximum depth of the feature with this dataset. The maximum contrast for the warm core is at approximately 400 mbar, being 1.0–1.5 K warmer than the coldest regions of the GRS in the east–west direction, and 3.0–3.5 K warmer than the coldest regions in the north–south direction.

Such large contrasts in the thermal field will have consequences for the wind field in the 100–500 mbar region. Visible imaging demonstrated that central parts of the GRS were largely quiescent, with ephemeral small-scale cyclonic vortices, organized eddy motion (Mitchell et al., 1981; Sada et al., 1996; Vasavada et al., 1998), and indications of counter-rotating flow (Vasavada et al., 1998; Choi et al., 2007). Most of the velocity and vorticity of the GRS is located in a thin anticyclonic ring at 70–85% of the radius (Sada et al., 1996; Simon-Miller et al., 2002). Under the assumptions of hydrostatic and geostrophic balance, the vertical shear on the tangential winds and the temperature gradient (measured radially outwards from the center of the GRS) are related by the thermal wind equation (see, e.g. Hanel et al., 2003). We take the tangential winds derived from Galileo Solid State Imager (SSI) data by Choi et al. (2007), and use them to integrate the thermal wind equation with altitude to generate the thermal wind cross-sections in the bottom panels of Fig. 5. The true altitude of the cloud-tracers for tangential wind determinations remains somewhat unclear. It is commonly assumed that tracers are all located at the same altitude, despite evidence for variable cloud-top topography from visible studies (Sada et al., 1996; Simon-Miller et al., 2002). We chose to place the wind field at a reference pressure of 700 mbar (the upper limit proposed by the vertical structure analysis of Simon-Miller et al. (2002)), though there is likely to be considerable uncertainty in this value across the GRS.

Choi et al. (2007) identified peak tangential velocities at  $16^\circ$  and  $24^\circ\text{S}$  in the north–south direction, and separated by  $14$ – $15^\circ$  in the longitudinal direction. Fig. 5 shows that the thermal gradients ensure that these peak tangential velocities decay with altitude into the lower stratosphere. The latitudinal cross-sections are particularly intriguing, as the temperature gradients imply that the location of these peak tangential velocities varies with altitude, moving south with increasing altitude. A similar southward displacement with altitude was observed in the location of the temperature minimum associated with the GRS core (in both the CIRs thermal maps presented here and in Simon-Miller et al. (2002)).

But the most striking feature of the thermal wind field is associated with the warm core of the GRS. The tangential velocities in Figs. 4 and 5 of Choi et al. (2007) indicate that velocities reach zero at  $20.5^\circ\text{S}$ , coincident with the latitude of the warm core. Furthermore, both their 1996 (G1) and 2000 (G28) Galileo results show

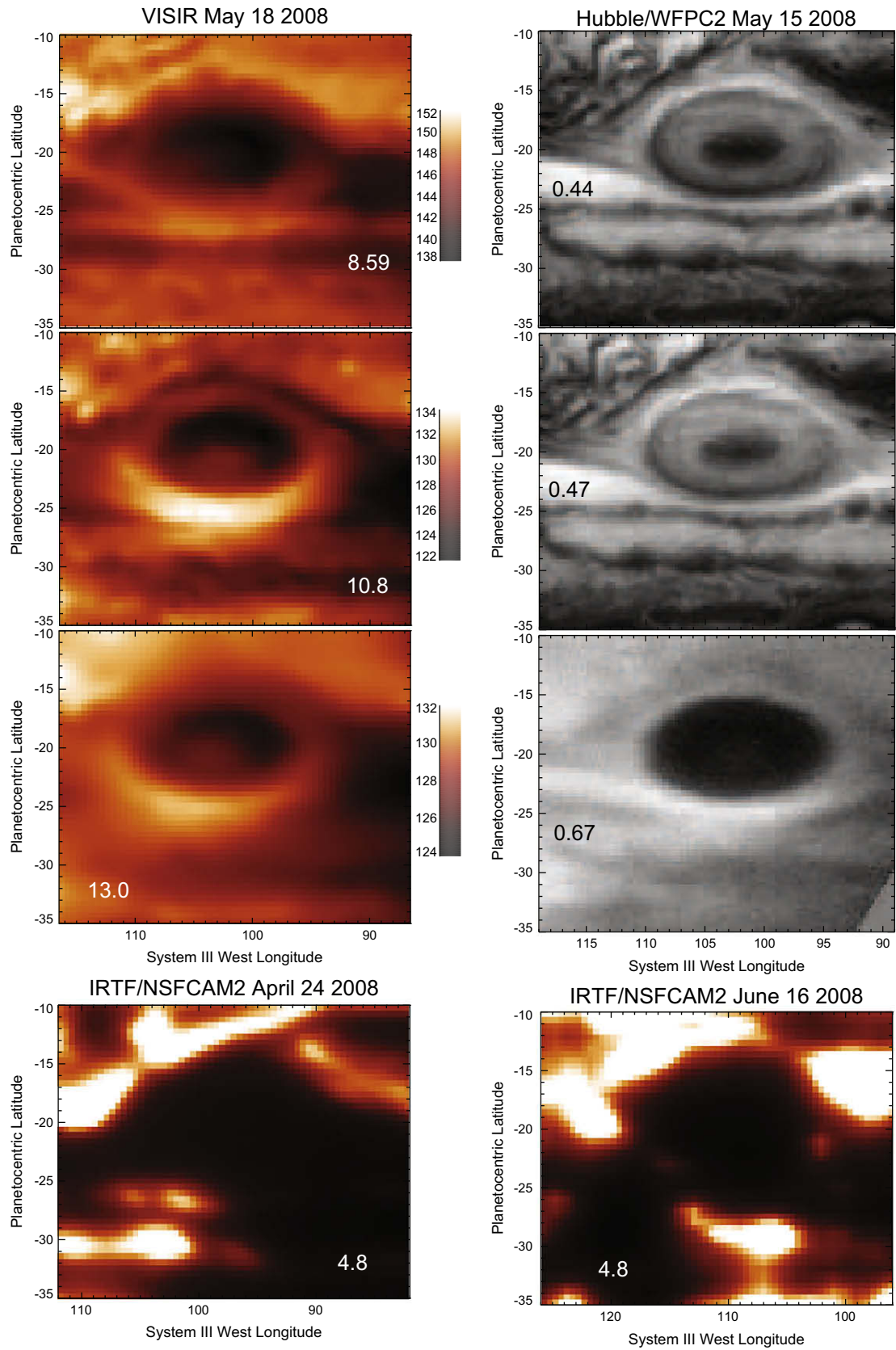


**Fig. 2.** Comparison of thermal imaging from VLT/VISIR (May 18th 2008), visible imaging from Hubble/WFPC2 (May 15th 2008) and IRTF/NSFCAM2 observations from April 24th 2008 and June 16th 2008, the closest dates available. The wavelength of each filter (in  $\mu\text{m}$ ) is given within each separate panel. The warm GRS core identified in Fig. 1 was also present in May 2008, suggesting that this is a long-lived and robust feature of the internal flow of the GRS.

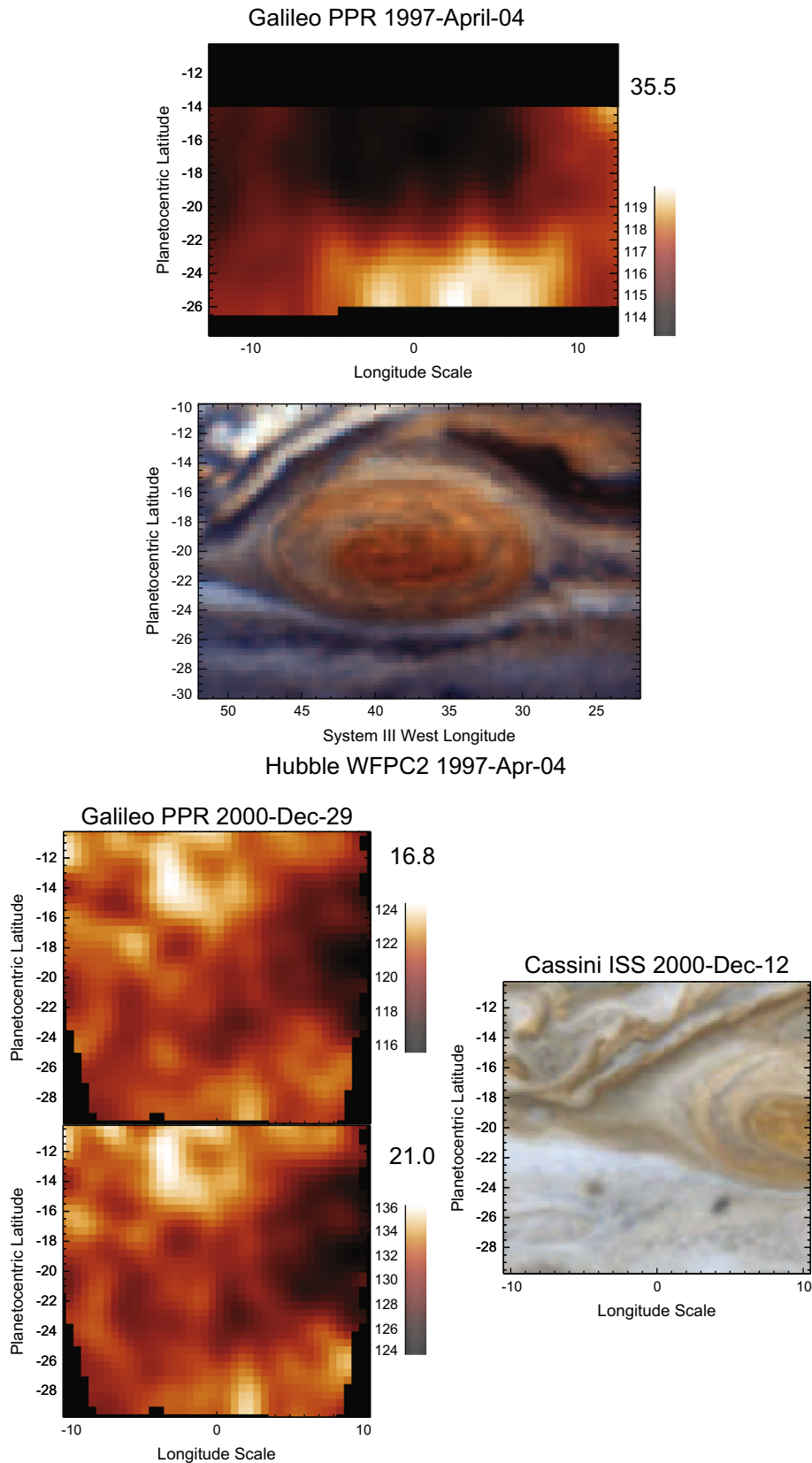


**Fig. 3.** Examples of the Galileo/PPR data (converted to brightness temperatures) acquired in 1997 and 2000. These can be compared to the only other Galileo observations of the GRS in Orton et al. (1996), which spanned a wider wavelength range (by 1997 Galileo/PPR was restricted to observing with only one or two filters) and had a lower spatial resolution. In the December 2000 imagery, the GRS is only partially observed on the right-hand side of each image. Visible imaging is shown for comparison to the thermal data. The Hubble/WFPC2 image from April 4th 1997 is a composite of images at 410 nm and 670 nm to show the deep red color of the center of the GRS. The Cassini/ISS image (Credit: NASA/JPL/Space Science Institute, image PIA07782, latitudes and longitudes are approximate) is a composite of 451 and 750 nm from Cassini's Narrow Angle Camera on December 12th 2000.

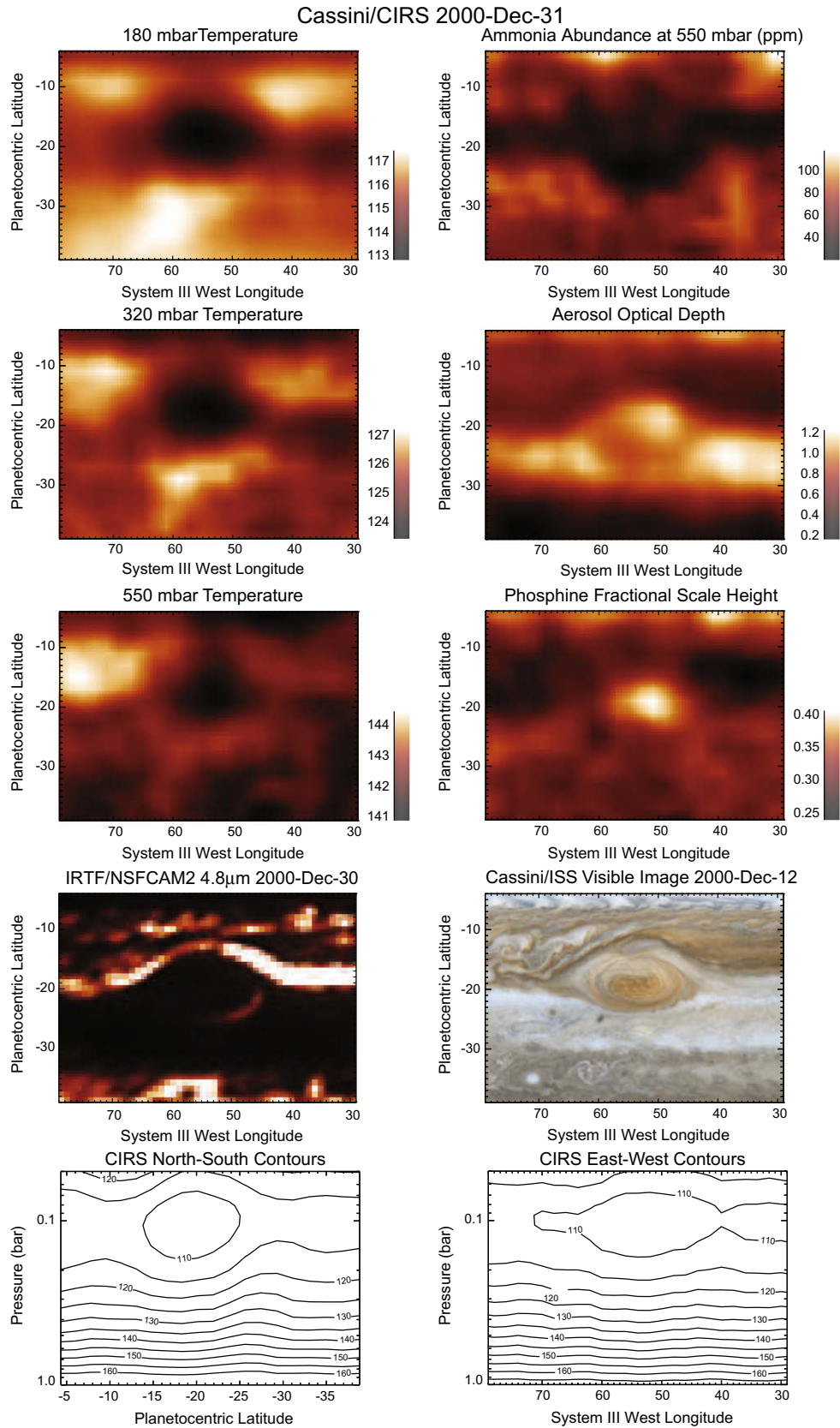


**Fig. 4.** Retrievals of tropospheric temperatures, abundances of  $\text{PH}_3$  and  $\text{NH}_3$  and the opacity of tropospheric hazes from Cassini/CIRS spectra between 600 and 1400  $\text{cm}^{-1}$ . The three panels on the top left show temperature maps with the GRS as a cold-core feature. Panels on the top right show the composition ( $\text{NH}_3$ , aerosols and  $\text{PH}_3$ ) from fitting CIRS spectra. The Cassini/ISS image (Credit: NASA/JPL/Space Science Institute, image PIA07782, latitudes and longitudes are approximate) is a composite of 451 and 750 nm images from Cassini's Narrow Angle Camera taken on December 11th–12th 2000. The IRTF/NSFCAM image on December 30 2000 is shown for comparison, stretched so that the fine-scale structure south of the GRS is revealed. The lower two panels are north–south and east–west slices through the GRS (with spectral information content covering the 75–800 mbar range). Retrievals were performed following Fletcher et al. (2009a) using the NEMESIS radiative transfer and retrieval model of Irwin et al. (2008).

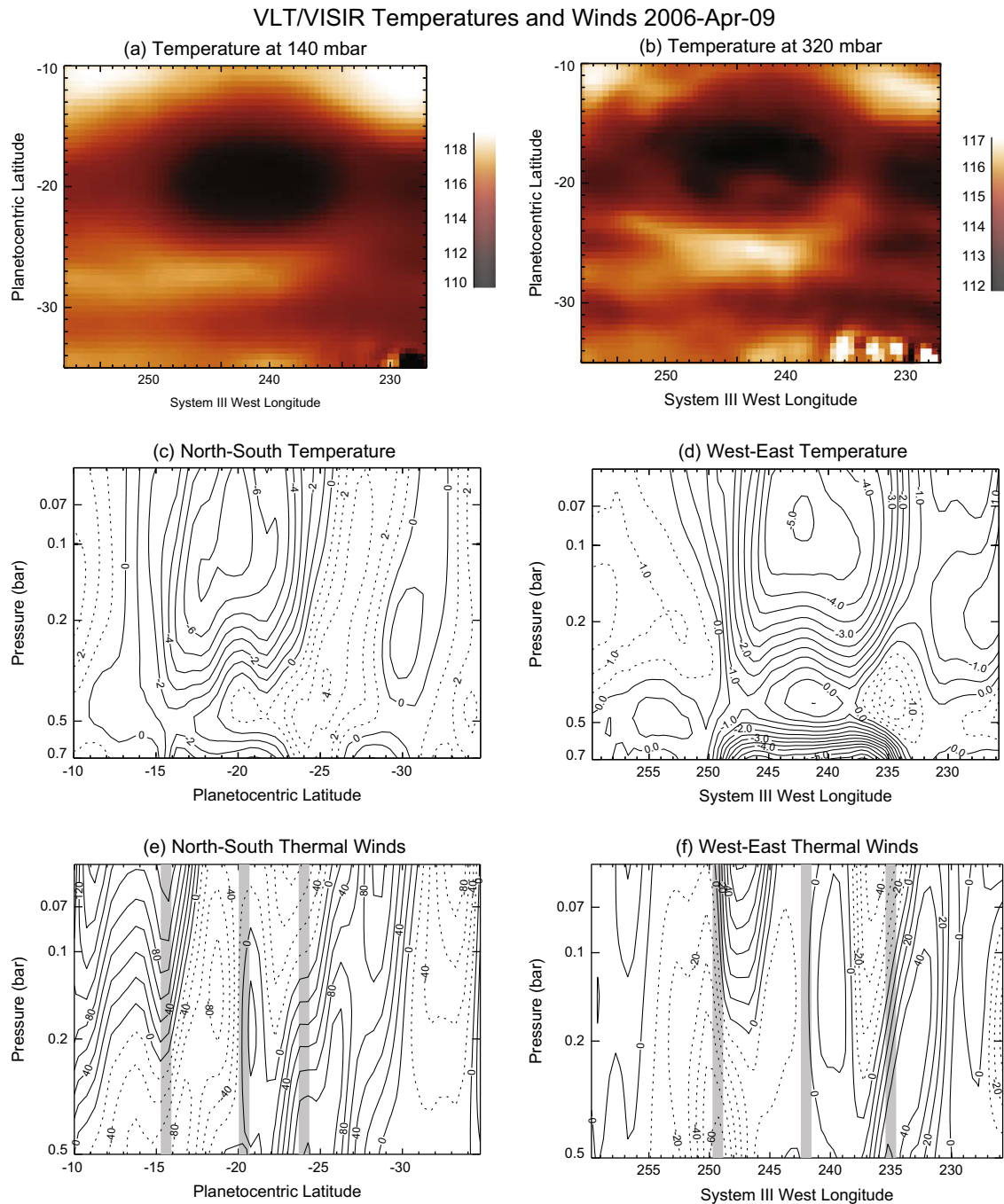


**Fig. 5.** Example of the temperatures and thermal winds derived from a single night of VLT/VISIR observations (April 9th 2006). (a and b) Temperature maps at 140 and 320 mbar, respectively, showing that the GRS warm core is more apparent at deeper pressures. Structure on the bottom right is due to bad pixels on the VISIR detector. In (c and d) we plot north–south and west–east contours through the center of the GRS, subtracted from a mean temperature field for the region surrounding the vortex. Dashed lines show temperatures warmer than the mean, solid lines show temperatures cooler than the mean. (e and f) Thermal wind calculations based on the tangential temperature gradients. The tangential winds of Choi et al. (2007) are placed at 700 mbar and integrated vertically using thermal shears deduced from the thermal wind equation. In (e) solid lines show prograde velocities, dashed lines show retrograde velocities. In (f) solid lines show northward velocities, dashed lines are southward velocities. The vertical gray bars denote the peak tangential winds and center of the GRS from Choi et al. (2007).

evidence for weak counter-rotation (clockwise); a cyclonic region within the anticyclonic vortex, extending over 3–4° latitude and 5–7° longitude. The thermal gradient introduced by the warm core implies that the peaks of the counter-rotation (at approximately 19 and 21°S) will also decay with increasing altitude into the lower stratosphere. The peak thermal winds at 100–200 mbar for the counter-rotation may be spurious, as it depends on the precise altitude of the cloud-tracers used to determine the tangential velocities within the GRS core. Although 6 years separate the VISIR and Galileo/SSI data, the size and location of the cyclonic region and

the warm atmospheric temperatures are in agreement. Unfortunately, wind measurements are not currently available in the 2006–2008 timeframe, so we cannot be certain that the counter-rotating flow or eddy motion persisted throughout this period.

#### 3.4. Spatial distribution of aerosol opacity

Jovian tropospheric aerosols provide broadband continuum opacity throughout the thermal-IR (Sada et al., 1996; Conrath et al., 1998; Wong et al., 2004; Matcheva et al., 2005), so that both

Cassini/CIRS (Fletcher et al., 2009a) and ground-based thermal imaging (Fletcher et al., 2009b) have been used to determine the meridional distribution of aerosols. In this section, we use the same techniques to retrieve spatially-resolved maps of the aerosol distribution in the region surrounding the GRS for comparison with visible observations.

Following the approach of Fletcher et al. (2009a) we placed a compact haze layer at 800 mbar with the broad spectroscopic features of NH<sub>3</sub> ice with 10- $\mu$ m particle radii, and varied the optical thickness to optimize the fit to the data. Figs. 4, 6, and 7 show retrieved temperature, aerosol and compositional maps from CIRS (December 31st 2000) and eight dates between April 9th 2006 and September 14th 2008 from VISIR and COMICS observations. In the absence of spectroscopically identifiable mid-IR features, we can make no deduction about the composition of the aerosols, so the opacity has been normalized to unity in ground-based retrievals because the retrieved parameter is only a proxy for the true horizontal distribution (Fletcher et al., 2009b). Furthermore, thermal-IR retrievals in the 7–25  $\mu$ m range cannot reliably distinguish between infrared opacity from the main cloud deck (seen at 4.8  $\mu$ m) and the overlying blue-absorbing tropospheric haze (Banfield et al., 1998; Fletcher et al., 2009a), so the aerosol opacity maps presented here contain no information on the vertical distribution of particulates.

The mid-IR aerosol opacities retrieved from both CIRS spectra and ground-based imaging show similar morphologies, despite the 6-year interval between observations. Opacity is highest over the GRS (also indicated by Voyager/IRIS retrievals, Sada et al., 1996), which is responsible for the absence of fine-scale structure in 4.8- $\mu$ m images of the GRS interior. However, the CIRS map (Fig. 4) suggests the GRS aerosols are indistinguishable from those in the rest of the STRZ to the south, with no detectable boundary between the two aerosol populations. And yet the two populations are known to be physically distinct. The methane-band 890 nm image in Fig. 1 shows that aerosols in the GRS interior reach considerably higher altitudes than the surrounding clouds.

The mid-IR aerosol opacities retrieved from both CIRS spectra and ground-based imaging show similar morphologies, despite the 6-year interval between observations. Opacity is highest over the GRS (also indicated by Voyager/IRIS retrievals, Sada et al., 1996), which is responsible for the absence of fine-scale structure in 4.8- $\mu$ m images of the GRS interior. However, the CIRS map (Fig. 4) suggests the GRS aerosols are indistinguishable from those in the rest of the STRZ to the south, with no detectable boundary between the two aerosol populations. And yet the two populations are known to be physically distinct. The methane-band 890 nm image in Fig. 1 shows that aerosols in the GRS interior reach considerably higher altitudes than the surrounding clouds.

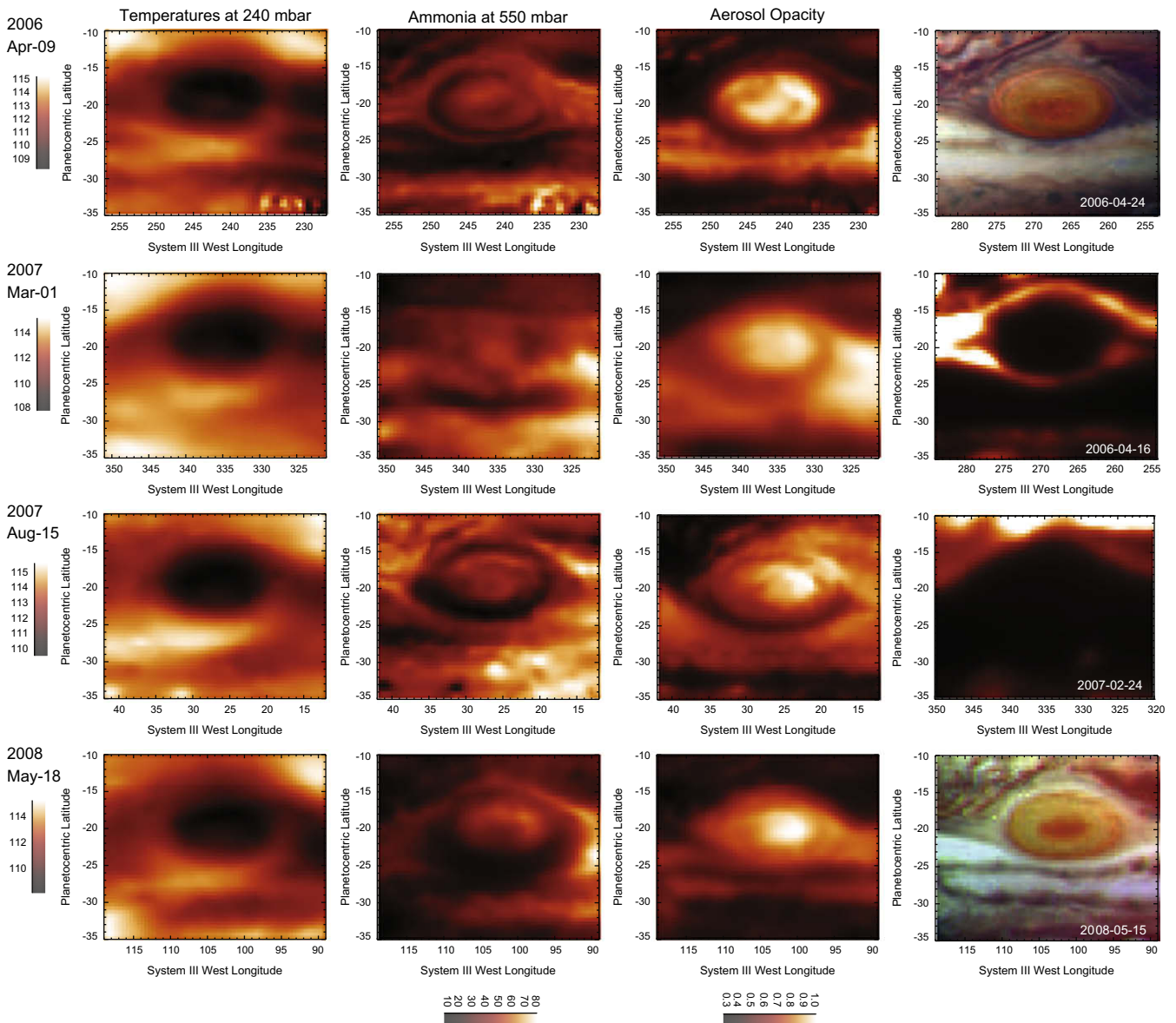


**Fig. 6.** Retrieval of atmospheric variables from VISIR data between April 2006 and May 2008. The three columns on the left show (a) temperatures, (b) ammonia at the peak of the contribution functions and (c) a proxy for the aerosol opacity. Ranges for each parameter are shown as legends to the left of the temperatures, and at the bottom for the composition. In the right-hand column, we compare the retrieved results to either visible imaging or 4.8  $\mu$ m imaging from IRTF/NSFCAM where available. The April 24th 2006 Hubble/ACS image is a composite of 0.33, 0.44 and 0.66  $\mu$ m visible images; the May 15th 2008 Hubble/WFPC2 image is a composite of 0.37, 0.47 and 0.50  $\mu$ m visible imaging.

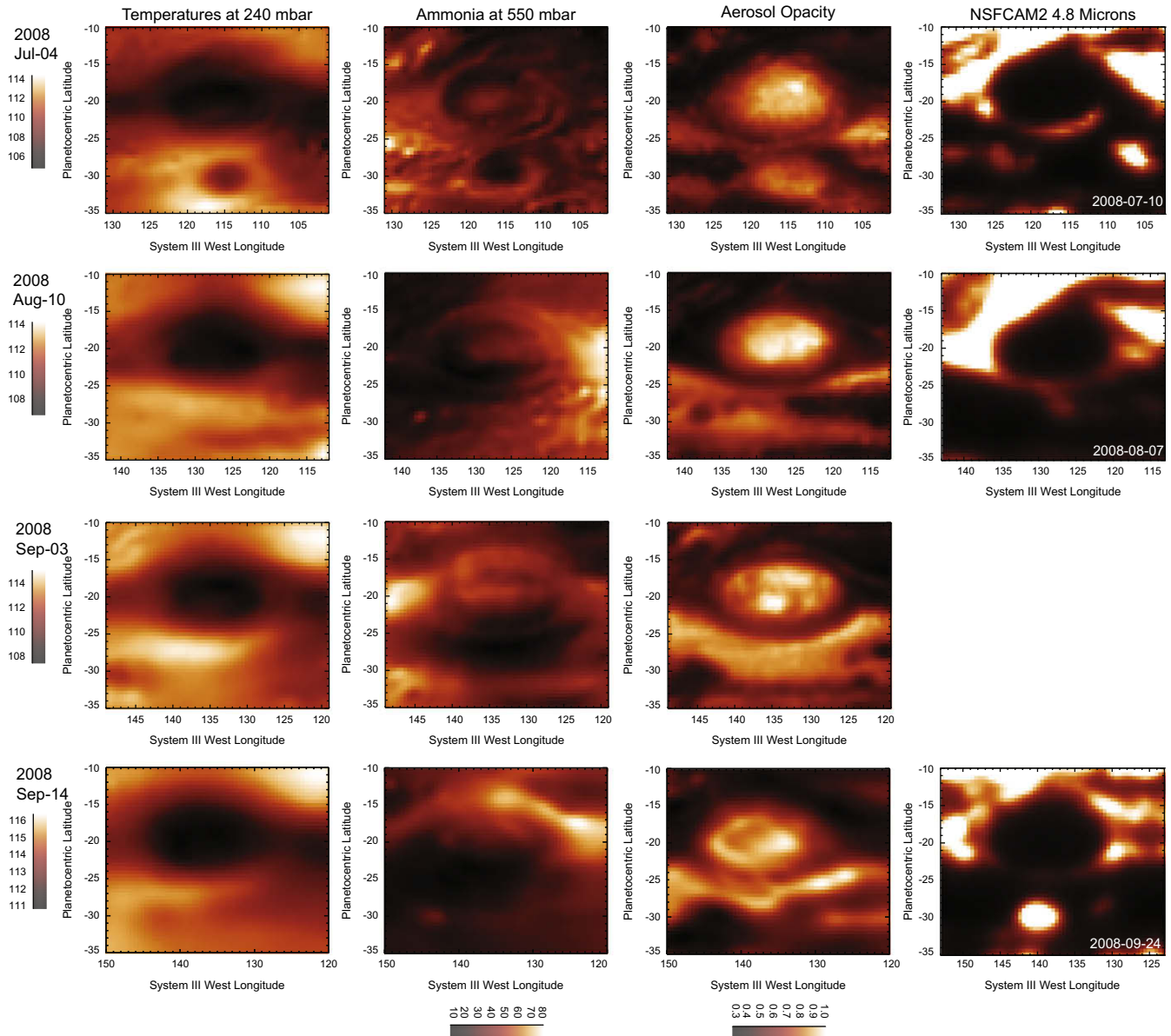


**Fig. 7.** Retrieval of atmospheric variables from VISIR and COMICS data between July and September 2008. The three columns on the left show (a) temperatures, (b) ammonia at the peak of the contribution functions and (c) a proxy for the aerosol opacity. Ranges for each parameter are shown as legends to the left of the temperatures, and at the bottom for the composition. In the right-hand column, we compare the retrieved results to 4.8  $\mu\text{m}$  imaging from IRTF/NSFCAM (where available).

And the Cassini/ISS image in Fig. 4 shows that the STRZ mid-IR aerosol opacity is coincident with an axisymmetric region of bright white clouds, whereas the GRS aerosols show different blue-red absorption properties, making them appear red. The separation of these two aerosol populations only becomes apparent in the VISIR and COMICS high-resolution retrievals, which resolve a narrow lane of low opacity between the GRS and the STRZ at 23–25°S. The low-opacity lane is compared with Hubble visible images in April 2006 and May 2008 in Fig. 6, and coincides with a dark region between the red and white aerosols. Furthermore, a similar dark lane at 25°S running east–west through the white aerosols south of the GRS, as well as the generally darker coloration of the turbulent SEB to the north, have low mid-IR aerosol opacities. Thus the darker clouds in visible imaging are relatively depleted in aerosol opacity at the altitudes sounded by mid-IR filters.

This depletion is usually associated with atmospheric subsidence, which would imply 4.8- $\mu\text{m}$  bright features due to an absence of attenuating aerosols (Terrile et al., 1979). This is

certainly the case for the ring of peripheral emission in April 2006 (compare the 4.8- $\mu\text{m}$  image, visible image and aerosol retrieval at the top of Fig. 6), suggesting that subsidence at the edge of the GRS penetrates from the tropopause down to the depth of 4.8- $\mu\text{m}$  cloud opacity (2–4 bars). Indeed, the low-opacity lane is coincident with the warm ring surrounding the GRS, indicative of atmospheric compression and warming at the vortex edges consistent with previous studies. However, the white aerosols of the STRZ completely attenuate 4.8- $\mu\text{m}$  radiance south of the GRS, and the dark lane through the middle does not have a 4.8- $\mu\text{m}$  bright counterpart, indicating that it resides above the main source of 4.8- $\mu\text{m}$  opacity. The temporal behavior of the peripheral ring will be discussed in Section 4.3.

In conclusion, thermal-IR aerosol opacity does not distinguish between red and white aerosols seen in visible imaging, but depletion in opacity is consistent with darker material seen at the GRS edges and in the SEB. A narrow lane of low mid-IR opacity, suggestive of strong subsidence, separates the aerosol populations of the GRS and the STRZ.

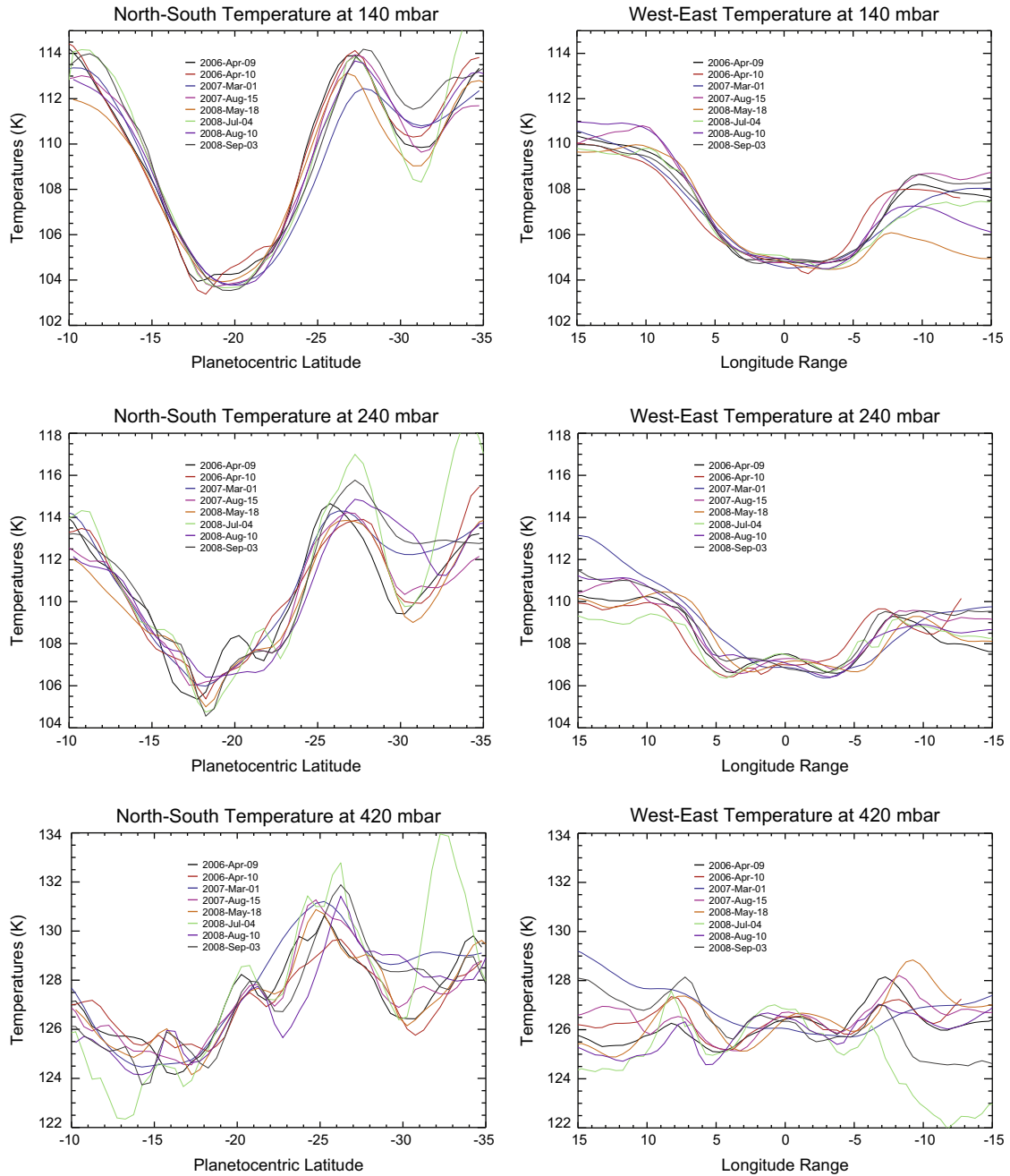


**Fig. 8.** Examples of north–south (left column) and east–west (right column) cut through the temperature structure derived from eight VLT/VISIR observations of the Great Red Spot. The three altitudes (140, 240 and 420 mbar) represent the range of altitudes where temperatures may be constrained independently of composition. Variations within the GRS core, the southern periphery, the location of the temperature minimum with latitude and pressure, and the east–west temperature contrast across the SEB are all described in the main text.

### 3.5. Compositional variations across the GRS

In addition to aerosols, spatial contrasts in gaseous composition ( $\text{PH}_3$ ,  $\text{NH}_3$  and para- $\text{H}_2$ ) derived from CIRS and ground-based imaging can be used to trace vertical motion in the jovian atmosphere.  $\text{PH}_3$  and  $\text{NH}_3$  were derived from CIRS spectra simultaneously with aerosol opacity for the first time (Fig. 4). The entire  $600\text{--}1400\text{ cm}^{-1}$  CIRS spectral range was modeled using the techniques described by Fletcher et al. (2009a), building on the work of Irwin et al. (2004) and Achterberg et al. (2006). For  $\text{PH}_3$  we fix the mole fraction below 1 bar to 1.9 ppm (Fletcher et al., 2009a) and vary only the fractional scale height  $f$ ; for  $\text{NH}_3$  we scale the saturated vapor pressure abundance to determine the mole fraction at 550 mbar

(the peak of the weighting function). As ground-based filtered imaging is insensitive to the distribution of  $\text{PH}_3$ , we scale the  $\text{NH}_3$  and aerosol distributions alone to match the VISIR imaging (Figs. 6 and 7). Finally, we present the first map of the para- $\text{H}_2$  fraction derived from the ground (Fig. 9, using COMICS imaging) for comparison with Voyager/IRIS results (Sada et al., 1996; Simon-Miller et al., 2002).

#### 3.5.1. Ammonia

The structure of the  $\text{NH}_3$  distribution in both CIRS (Fig. 4) and ground-based results (Figs. 6 and 7) is complex. Maximum information content arises from the 8 to 11  $\mu\text{m}$  filters, so results are quoted for 550 mbar, at an intermediate-altitude between the

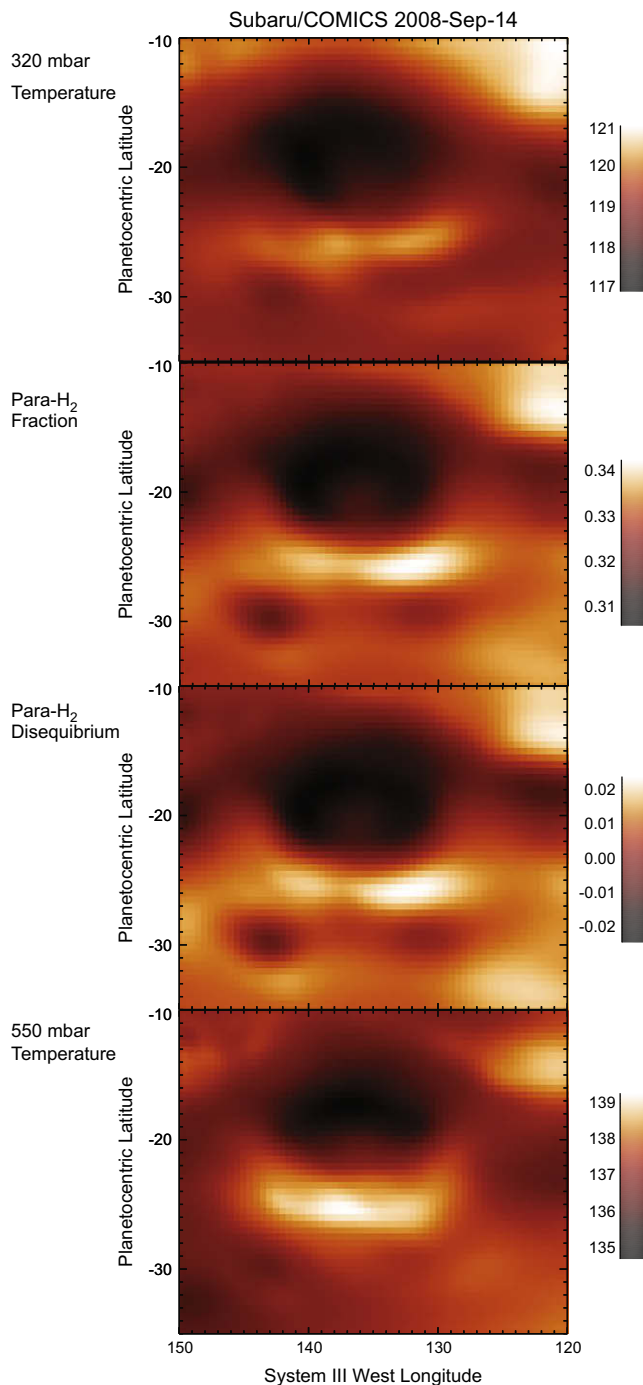


**Fig. 9.** Retrievals of temperature and the para-H<sub>2</sub> fraction from Subaru/COMICS observations on September 14th 2008. The maps at the top and bottom show the temperature field at 320 and 550 mbar. The para-H<sub>2</sub> fraction,  $f_p$  is given in the center two panels.  $T(p)$  was used to calculate the equilibrium para-H<sub>2</sub> fraction,  $f_{pe}$ , and the plot in the third row shows the extent of disequilibrium  $f_{pe} - f_p$  in the region surrounding the GRS. Sub-equilibrium conditions are indicative of upwelling, super-equilibrium conditions suggest subsidence.

peaks of the functional derivatives. Ammonia consistently shows a north–south asymmetry across the GRS, being elevated at the northern edge and in the vortex core ( $\approx 70$  ppm) and depleted towards the south in the location of the warm periphery ( $\approx 30$  ppm). Ground-based maps appear to show that NH<sub>3</sub> is more abundant north of the GRS core, but the spatial organization is particularly sensitive to (a) seeing variations on different dates, and (b) large uncertainties at high emission angles, when the GRS

was close to the planetary limb. But even though NH<sub>3</sub> retrievals from ground-based imaging appear variable from day to day, the large-scale trends (north–south asymmetry, peripheral depletion) are consistent between CIRS and ground-based datasets.

A similar north–south asymmetry was observed using IRTF spectroscopy (Lara et al., 1998), and the strong depletion of ammonia at the southern edge of the GRS indicates strong subsidence there. However, the depletion is typically over a wider latitude-range than both the narrow lane of depleted aerosol opacity discussed above and the narrow ring of 4.8- $\mu$ m emission (see the April 2006 results in Fig. 6, for example), with the NH<sub>3</sub> depletion extending well into the STrZ and south temperate belt (STB). The NH<sub>3</sub> abundance in the GRS interior is not significantly enhanced over the surrounding SEB and STrZ, but it is usually separated by a depleted region encircling the GRS, consistent with the model of strong subsidence at the edge. This distribution is consistent with the Voyager/IRIS determinations reported in Fig. 11 of Sada et al. (1996), but inconsistent with depletion in NH<sub>3</sub> above 350 mbar over the GRS (Griffith et al., 1992) from the same Voyager dataset.

### 3.5.2. Phosphine

The new CIRS results for PH<sub>3</sub> confirm previous work by Irwin et al. (2004), but with abundances which properly account for the distribution of aerosols. PH<sub>3</sub> is enhanced (fractional scale height  $f \approx 0.40$ ) in the northeast quadrant of the GRS, coincident with the coldest temperatures, but it is not equally enhanced everywhere across the vortex ( $f = 0.30$ – $0.35$ ) like the aerosol opacity. CIRS was the first instrument to demonstrate localized enhancement over the GRS (Irwin et al., 2004), as both Voyager/IRIS spectra in 1981 (Griffith et al., 1992) and IRTF spectroscopy in 1991 (Lara et al., 1998) indicated no PH<sub>3</sub> variations across the GRS region. We do not observe the 30% decrease in PH<sub>3</sub> abundance from 10 to 35°S described by Lara et al. (1998), but we note that these observations came shortly after the 1990 ‘global upheaval’ in which the SEB faded and later restored (Rogers, 1995), possibly associated with rapid vertical advection of PH<sub>3</sub> which could explain the difference between the 1991 and 2000 observations.

In conclusion, for both PH<sub>3</sub> and NH<sub>3</sub>, the highest concentrations are found to the north of the GRS center. It was noted earlier that the core of the GRS moves southwards with increasing altitude, so the PH<sub>3</sub> maximum could sit over the site of the most vigorous vertical mixing in the atmosphere beneath the visible cloud decks.

### 3.5.3. para-Hydrogen

Subaru/COMICS observed the GRS three times in 2008 (June 24th, September 14th and 15th), the latter two being sufficiently similar that only September 14th is shown at the bottom of Fig. 7. The GRS was too close to the planetary limb in the June 24th dataset, so that tropospheric temperatures were poorly constrained. Fig. 9 shows the vertical distribution of para-hydrogen on September 14th. The para-H<sub>2</sub> fraction may be separated from temperatures by comparing the relative populations of the S(0) and S(1) states (via comparisons of the 24.5- $\mu$ m filter with shorter wavelengths). Although Voyager/IRIS first demonstrated that the GRS exhibits a local minimum in para-H<sub>2</sub> (Sada et al., 1996; Simon-Miller et al., 2002), this is the first such map from the ground, and it has a significantly higher spatial resolution (Fig. 9). Using the derived  $T(p)$  structure to calculate the equilibrium para-H<sub>2</sub> fraction at every atmospheric level, we calculate  $f_p - f_{eqm}$  to show that the GRS interior is a region of sub-equilibrium conditions. This suggests that air parcels within the core are advected upwards at a faster rate than ortho-H<sub>2</sub> can be converted to para-H<sub>2</sub>, which is further evidence for strong convective updrafts in the center of the GRS. The strongest sub-equilibrium conditions are not exactly in the GRS center, but in the region away

from the warm core, towards the northern edge of the GRS. Conversely, super-equilibrium conditions dominate around the edge of the vortex (strongest at the southern edge), confirming the strong subsidence responsible for the periphery of warm temperatures and depleted ammonia and aerosols.

### 3.6. North–south asymmetry at the GRS periphery

When we combine the results of the previous sections, each of the species ( $\text{PH}_3$ ,  $\text{NH}_3$  and para- $\text{H}_2$ ) shows evidence for upwelling which is strongest towards the northern edge of the vortex near the SEB, away from the warm core region south of the geometric center. Similarly, the strongest depletions (and super-equilibrium para- $\text{H}_2$  conditions) are associated with an arc of warm air at the southern periphery (left-hand column of Figs. 6 and 7), south of the peripheral prograde jet at  $23.8^\circ\text{S}$  bordering the STrZ. And finally, the ring of  $4.8\text{-}\mu\text{m}$  emission shown in Figs. 6 and 7 is consistently darker at the southern edge than the northern edge, indicating greater attenuation of deep radiance in the south by a thicker aerosol layer.

Furthermore, the peak temperature of the southern arc is 8–10 K warmer than that of the cold core of the GRS, and 2–3 K warmer than the northern edge at 240 mbar. This thermal asymmetry between north and south was first noted in Galileo/PPR data (Orton et al., 1996), but is clearly evident in the April 1997 Galileo data (Fig. 3) and in the temperature retrievals from Cassini (Fig. 4). Fig. 5 shows that the location of the warm arc (and hence the peak thermal winds associated with the prograde velocities at  $23.8^\circ\text{S}$ ) moves southward with increasing altitude, to  $27\text{--}28^\circ\text{S}$  at 100 mbar. Thus the location of the cold airmass defining the interior of the GRS moves further south with increasing altitude above the cloud tops.

#### 3.6.1. The tilt of the GRS

The arc of warmer temperatures, super-equilibrium para- $\text{H}_2$  conditions, depleted  $\text{NH}_3$  and lane of low mid-IR aerosol opacity all suggest stronger atmospheric subsidence at the GRS periphery in the south than in the north. These compositional asymmetries may be related to a proposed ‘tilt’ in the GRS structure from north to south, suggested by previous authors using visible data. For example, Sada et al. (1996) suggested that the southern portion of the GRS collar flowed deeper in the atmosphere than the northern section to explain differences between Voyager 1 and 2 wind measurements; Simon-Miller et al. (2001) determined cloud heights to be at deeper pressures over the southern portion of the vortex; and shallow-water calculations of the bottom topography of the vortex using cloud-top velocities (Dowling and Ingersoll, 1989) suggest that the GRS is shallower in the north than in the south. From thermal-IR data, Simon-Miller et al. (2002) used Voyager/IRIS retrievals of temperature and para- $\text{H}_2$  to demonstrate a tilt of potential temperature surfaces. Plotting pressures on surfaces of constant potential temperature (surfaces of constant entropy, Read et al., 2006) then demonstrated the excursions of the flow streamlines from north to south.

A similar procedure is applied to ground-based temperature maps in Fig. 10. The specific heat capacity ( $c_p$ , calculated based on the rotational and translational contributions of ortho- $\text{H}_2$ , para- $\text{H}_2$ , He and  $\text{CH}_4$ ) varies from approximately 11.1 kJ/K at 1 bar to 9.9 kJ/K at the tropopause. This was used to calculate the potential temperature,  $\theta$ :

$$\theta = T(p) \left( \frac{p_0}{p} \right)^{(R/mc_p)} \quad (1)$$

where  $T$  and  $p$  are temperature and pressure, respectively;  $m$  is the mean molecular weight,  $p_0$  is a reference pressure of 1 bar and  $R$  is

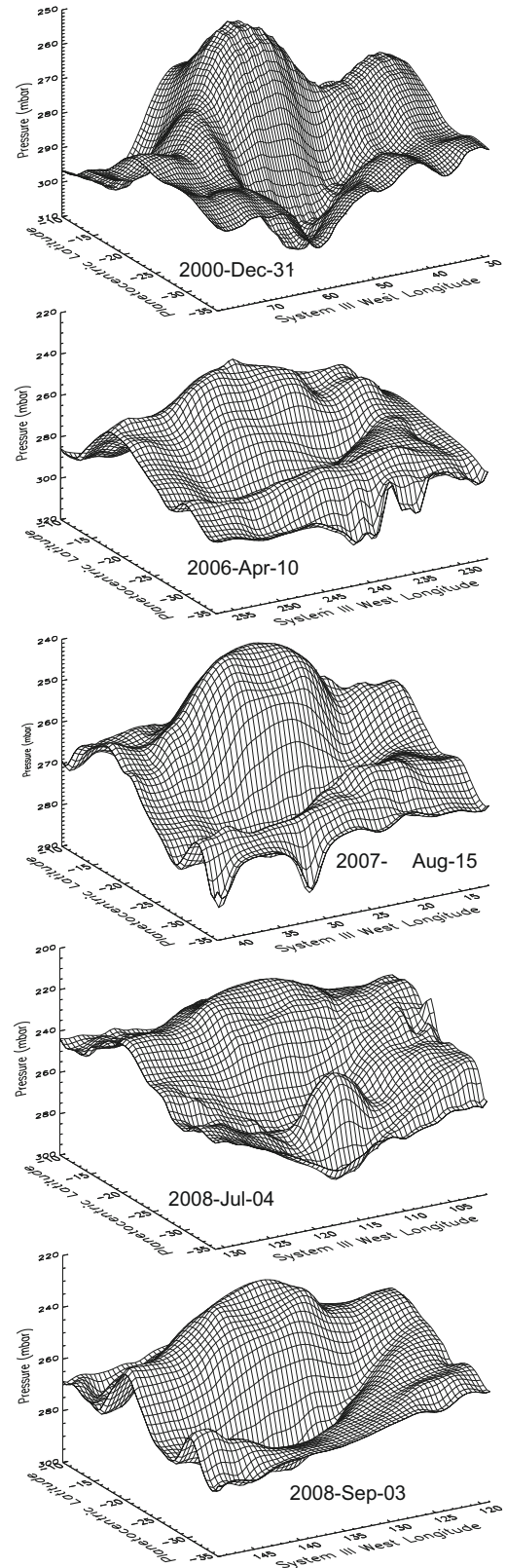


**Fig. 10.** Using the retrieved CIRS (top panel) and VISIR (bottom four panels)  $T(p)$  profiles to calculate the potential temperature,  $\theta$ , we then interpolate the pressure excursions onto the constant  $\theta = 185\text{ K}$  surface (approximately the peak of the Q-filter contribution functions) to show how pressure varies with location. The low-pressure (highest-altitude) GRS interior is modified by the warm core, and the pressure surfaces are visibly tilted from the SEB in the north to the STrZ in the south. In July 2008, the low-pressure core of Oval BA perturbed the surrounding atmosphere as it passed to the south of the GRS.

the molar gas constant, so that  $\theta$  varies from 170 K to 250 K between 1 bar and the tropopause. However, this equation for  $\theta$  is only strictly true for a constant para-H<sub>2</sub> fraction, as ortho and para-H<sub>2</sub> have different heat capacities and therefore different potential temperatures. Latent heat release from the conversion between ortho- and para-H<sub>2</sub> is not considered, so we are effectively assuming a ‘frozen’ composition at every level. Furthermore, because the thermodynamic effects of the ortho/para difference are relatively small for the warm temperatures of Jupiter (Simon-Miller et al., 2002), we found that similar results were obtained whether we used (a)  $f_p = 0.25$  everywhere (the high temperature limit), (b) the retrieved  $f_p$  values from Subaru/COMICS, or (c) the equilibrium value  $f_{eqm}$ . Differences were smaller than the uncertainties associated with the  $T(p)$  retrievals from ground-based data. We used this equation to interpolate pressures onto  $\theta$  surfaces ( $\theta = 185$  K in Fig. 10) to visually represent the high altitude (upwelling, low pressure) and low altitude (subsiding, high pressure) excursions of the pressure levels surrounding the GRS.

The four plots in Fig. 10 confirm the north–south tilt of the pressure excursions inferred from Voyager/IRIS data by Simon-Miller et al. (2002). The GRS reaches to the highest altitudes over the spatial range considered (consistent with numerous visible studies, see e.g. Sada et al., 1996), and the warm central feature is evident as a small hollow in the pressure surfaces in the GRS center. The highest altitudes are reached to the north of the GRS (consistent with maxima in PH<sub>3</sub> and NH<sub>3</sub>, and with elevated cloud tops inferred by Simon-Miller et al. (2001)). The north–south tilt is time-variable, and particularly sensitive to the passage of anticyclones south of the GRS, to be discussed in Section 4.2. In summary, we find that temperature and compositional maps of the GRS show north–south asymmetries which are related to the tilt of streamlines inferred from visible analyses. A high-pressure core situated beneath the northern region of the GRS interior could result in vigorous upwelling, resulting in the distribution of tracers and the elevated pressure surfaces towards the northern edge of the GRS. These asymmetries will provide an important challenge for the next generation of dynamical models of the GRS.

### 3.7. Turbulence in the SEB

The final conclusions regarding the atmospheric structure focusses on the region of turbulence to the northwest of the GRS. The high spatial resolutions offered by the Galileo/PPR (December 2000, Fig. 3) and ground-based data (Figs. 6 and 7) allow us to observe thermal contrasts within this region for the first time. At lower spatial resolutions (e.g. the CIRS thermal maps in Fig. 4), the SEB is characterized as a simple warm belt, albeit with a contrast in temperatures between east and west of the GRS which is larger with increasing depth into the troposphere. At 550 mbar, the SEB northwest of the GRS is the warmest region in the spatial range considered (Fig. 4). Compositional retrievals show the mid-IR aerosol opacity is lower over the SEB than the GRS and STRZ to the south, and para-H<sub>2</sub> is close to its equilibrium value over the SEB (Fig. 9). The SEB is generally bright at 4.8- $\mu$ m, particularly close to the GRS periphery where subsidence and cloud clearing is expected to be strongest. Furthermore, PH<sub>3</sub> is relatively depleted over the SEB compared to the STRZ, showing the typical belt/zone behavior.

Unfortunately, thermal and visible imaging were never taken on the same day, and the chaotic structures within the SEB are known to move and evolve over rapid timescales. Nevertheless, both PPR and ground-based data show discrete regions of warmer temperatures, elevated aerosol opacities and NH<sub>3</sub> abundances (see July 4th 2008 in Fig. 7, for example). The NSFCAM2 observation (6 days later, in Fig. 7) shows that the aerosols northwest of the GRS are attenuating 4.8- $\mu$ m flux from the deeper atmosphere. The chaotic structure in the turbulent SEB is one of the only regions on the pla-

net known to produce spectroscopically identifiable but short-lived NH<sub>3</sub>–ice clouds (SIACs, Baines et al., 2002, 2007; Reuter et al., 2007), and the discrete features in the NH<sub>3</sub>–gas, temperature and mid-IR aerosol opacity maps are likely related to this strong upwelling motion taking place deep within the belt. Furthermore, the equilibrium para-H<sub>2</sub> fraction might represent a balance between large-scale subsidence over the belt (responsible for the higher atmospheric temperatures and aerosol-free conditions) and small-localized upwelling events dredging up low- $f_p$  air from depths. Conditions within the SEB are known to be time-variable (Section 4.4), so we now turn to a discussion of temporally evolving phenomena in the next section.

## 4. Results II: temporal variability of the Great Red Spot

The second aim of this study was to use thermal-IR imaging to constrain the temporal variation of the atmospheric temperature and composition within and surrounding the Great Red Spot. The ground-based observations, from observatories with both 3-m and 8.2-m primary mirrors, are used to provide context for the ‘snapshots’ obtained from visiting spacecraft (Galileo, Cassini and New Horizons, in particular). We surveyed thermal-IR and 4.8- $\mu$ m imaging from NASA/IRTF from 1995 to 2008. Fig. 11 shows 20 examples of the brightness temperatures at 17.9  $\mu$ m (sensitive to temperatures at 240 mbar) between July 8th 1995 and May 30th 2007. Fig. 12 shows 20 examples of brightness at 4.8  $\mu$ m (warm flux from the several-bar level attenuated by clouds and hazes above) between July 18th 1999 and September 24th 2008. Compared with the mid-IR images, the 4.8- $\mu$ m maps have an intrinsically better diffraction-limited spatial resolution, and show fine-scale structure surrounding the GRS. These complement the retrieved quantities from 8.2-m observations (2006–2008, Figs. 6 and 7), and are supplemented by TReCS thermal imaging at the time of the New Horizons encounter (February 2007, Fig. 13, discussed below).

At first glance, these figures demonstrate the remarkable stability of the GRS in the thermal-IR (despite the surrounding turbulence) as it moves slowly westwards with the zonal flow, but several variable phenomena are described below.

### 4.1. Variability of the warm core of the GRS

Fig. 5 depicts the north–south and east–west retrieved temperatures from the VISIR dataset between 2006 and 2008. The warm core region is not a static feature, but is observed to move in latitude and longitude with time. There is no noticeable periodicity to the motion, nor did we find evidence for responses to forcings external to the GRS. As the radial temperature gradients within the GRS vary, this must also mean that the vertical shear on the tangential velocities in the interior is variable. Indeed, the extent of counter-rotation within the GRS center varied between Voyager and Galileo G1 and G28 measurements (Choi et al., 2007), and contemporaneous thermal and cloud-tracked wind measurements would be important to verify the connection between the warm temperature core and the counter-rotating flow. The warm core was identifiable throughout the 2006–2008 period (including the TReCS observations in 2007, Fig. 13), and although the lower-resolution IRTF observations are unable to confirm its presence during the Galileo and Cassini encounters, we predict that this is a reasonably stable feature of the GRS.

### 4.2. Southern warm anomaly

The southern warm arc on the GRS periphery is well defined and symmetric in the east–west direction in N-band (7–14  $\mu$ m)

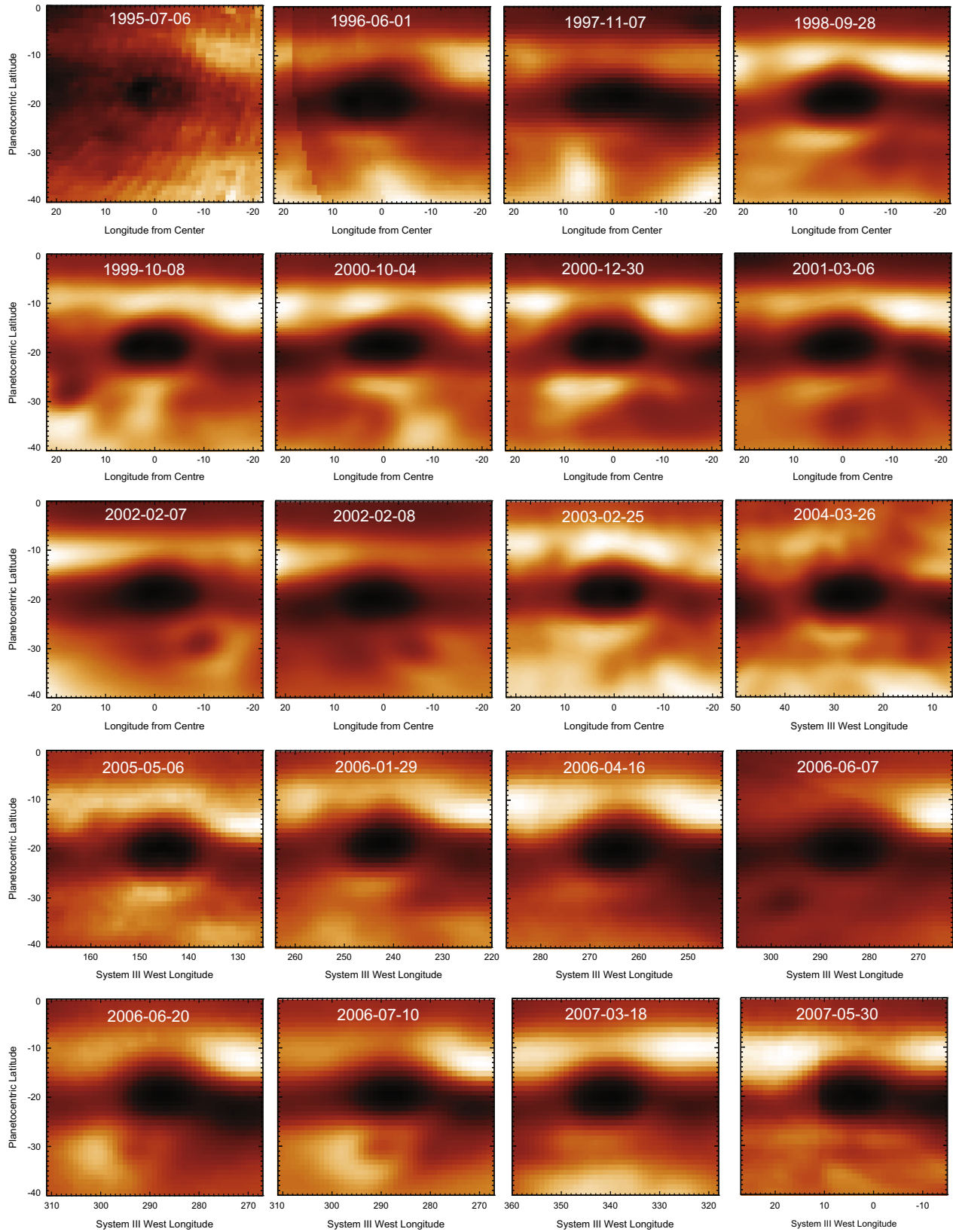


**Fig. 11.** The evolution of the GRS and its surrounding atmosphere from 1995 to 2007, imaged at 17.9  $\mu\text{m}$  (sensitive to 240 mbar temperatures) using the MIRLIN and MIRS instruments of the NASA IRTF. MIRLIN images suffered from an erroneous timestamp which prevented us from accurately determining longitudes, so the x-axis refers to a longitude scale referenced to the center of the GRS. The brightness temperature scales range from 108 to 119 K, consistent with the Galileo/PPR data in Fig. 3. IRTF monitoring allows us to track north–south and east–west variations in temperature, especially in response to the close passage of vortices in the STB, but cannot resolve structure internal to the GRS.

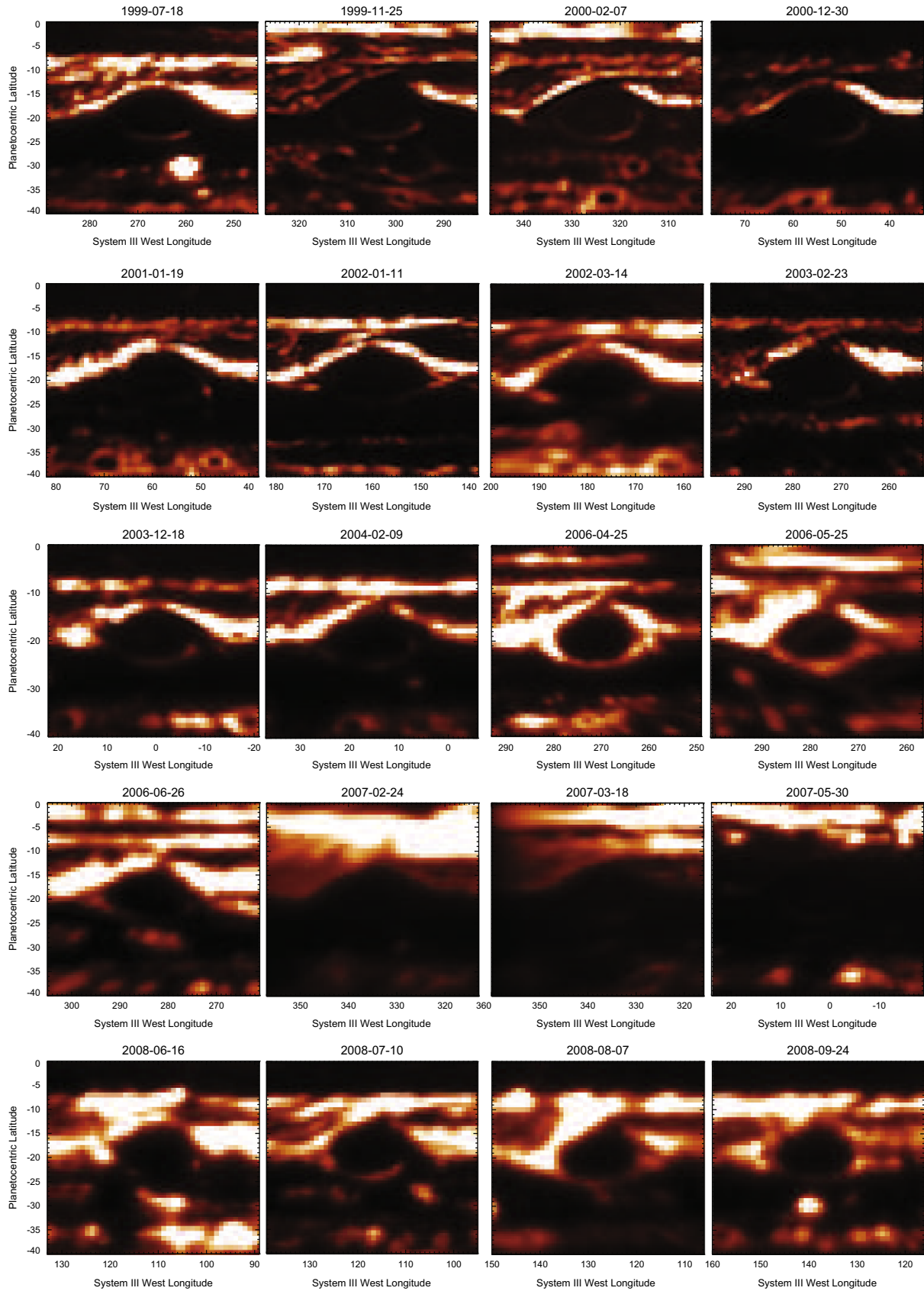


**Fig. 12.** The 4.8- $\mu\text{m}$  flux from the GRS region over the past decade, from 1999 to 2004 using NSFCAM and from 2006 to 2008 using NSFCAM2 at the NASA/IRTF. This wavelength is sensitive to the thermal emission from the several-bar level, attenuated by overlying clouds and hazes, so can be interpreted as a map of aerosol opacities. The images have been stretched so that bright SEB and equatorial features do not wash out dimmer features (such as the ephemeral bright ring of emission surrounding the GRS).

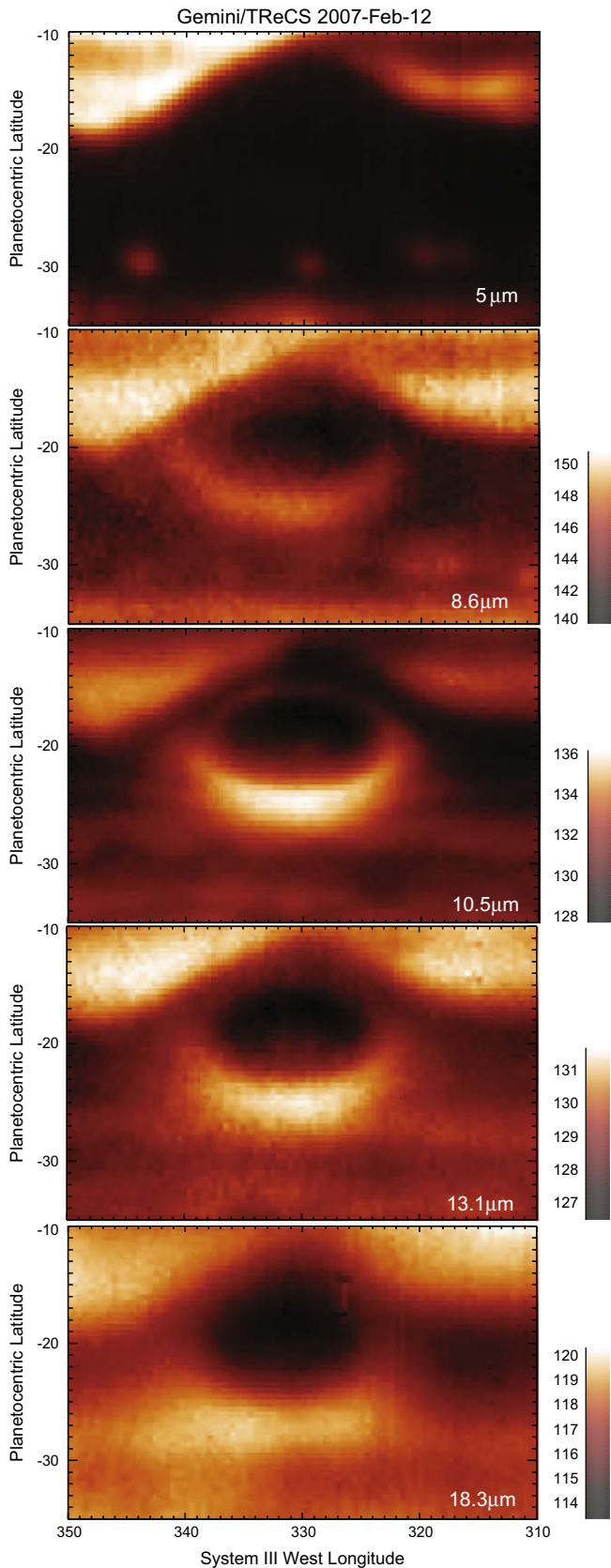


**Fig. 13.** Gemini/TReCS infrared imaging of the Great Red Spot on February 12th 2007, shortly before the New Horizons encounter. Five filters (5.0, 8.6, 10.5, 13.1 and 18.3  $\mu\text{m}$ ) are shown here. With only a single Q-filter at 18.3  $\mu\text{m}$ , these data are unsuitable for the full temperature and composition retrieval, but do provide additional information about the morphology of the vortex.

filtered imaging (sensitive to deep temperatures, ammonia and aerosol opacity, Figs. 1, 2 and 13). However, in Q-band (17–25  $\mu\text{m}$ ) filters, which sense higher altitudes, an ephemeral phenomenon can be seen extending from the southern periphery towards the southwest, referred to here as the Southern Warm Anomaly, or SWA. The SWA is a region of enhanced temperatures extending southwestward towards the warm South Temperate Belt (STB), sheared by the retrograde jet at 28.7°S (Porco et al., 2003). The detection in the Q-band filters, and the retrievals from Cassini/CIRS spectra in December 2000 (Fig. 4), suggests this phenomena exists in the 100–400 mbar region of the upper troposphere. There are no counterparts in the visible imaging, 4.8- $\mu\text{m}$  imaging or compositional retrievals, suggesting that this is purely a thermal effect, occurring at altitudes above the clouds responsible for 4.8- $\mu\text{m}$  opacity.

Fig. 11 indicates that the SWA is an ephemeral phenomenon, and that it is perturbed by interactions with passing anticyclones in the STB. Oval BA formed from the successive mergers of white Ovals BC and DE in 1998, and then BE and FA in 2000 (Sanchez-Lavega et al., 2001). The white oval then reddened in late 2005, and is presently the second largest red anticyclone in the jovian atmosphere (Simon-Miller et al., 2006). The zonal velocities of Oval BA and the GRS are such that they undergo close encounters approximately once every 2 years (García-Melendo et al., 2009), and the mid-IR dataset captured three of these encounters in February 2002, July 2006 and July 2008. Shallow-water dynamical simulations suggest that strong interactions between the GRS and BA are unlikely because the zonal jet systems do not permit perturbations to the central latitudes of the two vortices (García-Melendo et al., 2009). However, the warm airmass south of the GRS is absent when the cold airmass over Oval BA (due to upwelling and expansion in the vortex core) passes through the STB beneath the GRS. For example, the February 2002 encounter (3rd row of Fig. 11) removed the SWA, replacing it with a cooler region as the white Oval BA passed. The warm periphery had been present a year earlier (between at least March and October 2001), and was reestablished a year later (by February 2003). The July 2006 and July 2008 interactions (bottom row of Fig. 11, top row of Fig. 7) were notably different in the thermal-IR, as the reddened Oval BA exhibited its own warm southwestern anomaly.

The 2008 encounter was observed by VLT/VISIR, and retrieved parameters in the top panel of Fig. 7 indicate that BA shares many of the characteristics of the GRS – elevated mid-IR aerosol opacities, cold internal temperatures, and a warm southern periphery. BA is dark at 4.8- $\mu\text{m}$  because of the attenuating aerosols, but lacks the external ring of emission and depleted  $\text{NH}_3$  characteristic of the GRS. The central upwelling is shown dramatically in Fig. 10 as a disruption to the normal depth of the pressure contours at the southern edge of the GRS. Although we see no perturbations to the internal thermal structure and composition of either vortex during the interactions (confirming the predictions of García-Melendo et al. (2009)), it is clear that the southern warm airmass of the GRS, associated with strong subsidence at its periphery, is perturbed by encounters with the cold-core Oval BA. Furthermore, these encounters alter the north–south asymmetry in the GRS temperature structure (e.g. Fig. 8 shows that the regions south of the GRS and north of the prograde jet at 32.5°S vary by up to 4 K during the 2-year study), and hence the tilt of the pressure surfaces as shown in Fig. 10. Such variability could explain the shifting asymmetry in tangential windspeeds between the northern and southern edges of the vortex between the Voyager and Galileo eras (Choi et al., 2007).

#### 4.3. Changing visibility of the GRS periphery

Aside from the ephemeral SWA in the 100–400 mbar region, the effects of subsidence at the GRS periphery vary in their visibility

with time. The 4.8- $\mu\text{m}$  maps in Fig. 12 indicate that the bright peripheral emission can appear as a complete ring (February 2000, April 2006, June–August 2008) or be absent completely (February–May 2007). A break in the emission ring is sometimes apparent at the northernmost edge of the GRS (e.g. third row of Fig. 12), due to a streak of clouds or hazes separating the northeastern and northwestern regions of the flow in the SEB. Furthermore, the retrieved aerosol opacities from 2006 to 2008 (Figs. 6 and 7) show that the lane of low mid-IR opacity, which separates the GRS and STrZ aerosol populations, varies in width and thickness with time. The ring of depleted  $\text{NH}_3$  identified above is similarly ephemeral, being present when upper tropospheric aerosols demonstrated clear separation from the STrZ (April 2006, August–September 2008) and absent when the aerosols were more diffuse (February–March 2007).

Both the ring of bright 4.8- $\mu\text{m}$  emission and the depleted  $\text{NH}_3$  opacity are related to subsidence and cloud-clearing in the deep cloud layers, but their month-to-month visibility are correlated with the changing distribution of aerosol opacity in the upper troposphere. When the mid-IR aerosols were diffuse and no clear separation between GRS and STrZ aerosols was observed (February–March 2007, Fig. 6), the bright 4.8- $\mu\text{m}$  ring was obscured (Figs. 12 and 13). Similarly, when the bright 4.8- $\mu\text{m}$  ring was readily visible (July 2008), there was a clear lane of depleted mid-IR aerosol opacity in the retrievals (Fig. 7). Given the long-term stability of the GRS meteorology, the peripheral subsidence is likely to be a permanent feature, albeit temporarily obscured by overlying aerosols.

#### 4.4. Turbulent regions of the SEB

Visible imaging from Smith et al. (1979), Porco et al. (2003) and Vasavada et al. (1998, 2002) showed the ever-changing structure of the turbulent region of the SEB northwest of the GRS (the NWTR), and it was noted in Section 3.7 that the small-scale structures observed in the temperatures, aerosol opacity and  $\text{NH}_3$  distributions were varying with time. Indeed, these features evolve over time spans of hours and days, and the ground-based dataset has insufficient temporal sounding to study the evolution of the discrete convective events. However, the morphology of the turbulent region was particularly noteworthy during the New Horizons encounter in February 2007 (Baines et al., 2007; Reuter et al., 2007), when it appeared unusually quiescent and free of convective activity.

Typically, the brightest 4.8- $\mu\text{m}$  emission is found in the turbulent region close to the strong retrograde jet at 17.5°S (Fig. 12). However, the 4.8- $\mu\text{m}$  brightness was unusually subdued from February to May 2007, suggesting higher cloud opacities in the deep atmosphere than normal. This enhanced attenuation could be due to a shift in the usual balance between large-scale subsidence (resulting in the warm temperatures and low tropospheric haze opacities) and localized upwelling events (the fine structure typically observed in the  $\text{NH}_3$  and aerosol retrievals in Figs. 6 and 7). This is consistent with the absence of small-scale convection, generating fewer holes in the ubiquitous cloud layer so that (a) less 4.8- $\mu\text{m}$  flux can penetrate through, and (b) fewer bright white clouds appear at high altitudes, making the entire region appeared dark in color (Baines et al., 2007). The ultimate cause of the subdued convective activity remains unknown, but the unusual behavior could be related to the SEB color-fading in early 2007. This coincided with the cessation of the usual convective activity, and was followed by an outbreak in May 2007 and subsequent revival (darkening) of the SEB during a period of ‘global upheaval’ (Rogers, 2008; Go et al., 2008).

It is interesting to note that no major changes were apparent in either the thermal field in the 100–200 mbar range or the mid-IR

aerosol opacities during the New Horizons encounter (fifth row, Figs. 11 and 6). Furthermore, IRTF and Cassini thermal imaging (Figs. 11 and 4) demonstrate a shifting asymmetry in the SEB temperatures to the northwest and northeast of the GRS throughout the 1995–2008 timeframe which have no obvious counterparts in visible or 4.8- $\mu\text{m}$  imaging. As both the retrieved temperatures and mid-IR aerosol opacities are sensitive to conditions in the troposphere well-above the sources of 4.8- $\mu\text{m}$  opacity, it is reasonable to conclude that the visible and near-IR changes during 2007 were confined to pressures greater than 500–700 mbar.

## 5. Discussion and conclusions

Ground-based thermal-IR imaging of Jupiter from observatories with 8.2-m primary mirrors, with their broad wavelength range and temporal coverage, provide diffraction-limited spatial resolutions that surpass the capabilities of visiting spacecraft. These high spatial resolutions permit the first direct comparisons of visible cloud structures and thermal retrievals of temperature, aerosol opacity and gaseous composition within and surrounding the Great Red Spot. The aims of this investigation were twofold: (a) to use the spatial distributions of temperature, aerosols and composition as tracers of atmospheric dynamics within the vortex; and (b) to quantify atmospheric changes to the GRS and its surrounding atmosphere with time. Thermal and compositional mapping from a combination of Galileo, Cassini, NASA/IRTF, VLT, Subaru and Gemini observations were used to provide new insights into the structure, dynamics and stability of the GRS, detailed in the list below.

1. *GRS core*: A coherent warm core, extending over 8° of longitude and 3° of latitude, was observed within the cold anticyclonic vortex at 21°S throughout the 2006–2008 period of high-resolution observations. The maximum contrast between the core and the coldest regions of the GRS was 1.0–1.5 K in the east–west direction, and 3.0–3.5 K in the north–south direction at 400 mbar, although the warmer temperatures are present throughout the 150–500 mbar range. The resulting thermal gradients imply that any counter-rotation within the GRS interior (Choi et al., 2007) will despin with altitude into the lower stratosphere. The warm core is correlated with the deepest red coloration of the GRS interior in Hubble observations, suggesting a dynamical or chemical link between temperature and the red GRS aerosols. We speculate that variability in this warm core prior to 2006 was responsible for variations in the GRS flow at its center observed in Voyager and Galileo tangential velocity measurements.
2. *Tropospheric haze*: Spatially-resolved maps of mid-IR aerosol opacity surrounding the GRS were retrieved from Cassini/CIRS and ground-based imaging for the first time. These revealed a well-defined lane of low opacity at the southern periphery of the GRS, consistent with a narrow region of atmospheric subsidence, that separates the red aerosols in the GRS from the white aerosols of the STrZ. Red and white aerosols are otherwise indistinguishable at mid-IR wavelengths. Visibly-dark material at the GRS periphery and within the SEB coincide with regions of low mid-IR aerosol opacity, and the distribution of this upper tropospheric haze modulates the visibility of the bright peripheral ring of 4.8- $\mu\text{m}$  emission from the deeper troposphere.
3. *Compositional asymmetries*: Maps of  $\text{NH}_3$ ,  $\text{PH}_3$  and para- $\text{H}_2$  all show evidence for the highest concentrations (or, in the case of para- $\text{H}_2$ , the most sub-equilibrium conditions) towards the northern edge of the vortex center (north of the warm vortex core, closest to the SEB), with the strongest depletions in a symmetric arc at the southern periphery near the STrZ, coincident

with the warmest temperatures. In addition, 4.8- $\mu\text{m}$  maps of cloud opacity are consistently darker at the southern periphery than at the north, indicating greater attenuation of flux by a thicker cloud layer. These north–south compositional asymmetries are likely to be related to the proposed ‘tilt’ of the GRS structure deduced from visible cloud-tracking (e.g. Simon-Miller et al., 2002). A high-pressure core situated beneath the northern edge of the GRS interior would produce vigorous upwelling in the north and stronger subsidence in the south, resulting in the spatial distribution of tracers reported here. These asymmetries will provide an important challenge for the next generation of GRS dynamical models.

4. *Changes in the SEB*: The SEB is characterized by warm temperatures and low aerosol opacities, in addition to near-equilibrium para- $\text{H}_2$  fractions suggestive of a balance between large-scale subsidence (typical belt-like behavior) and localized upwelling events. Maps of  $\text{NH}_3$  and mid-IR aerosol opacity show small-scale enhancements in the turbulent region northwest of the GRS which correspond to dark structures at 4.8  $\mu\text{m}$ , likely related to the convection responsible for spectral identifications of  $\text{NH}_3$  ice in the SEB (Baines et al., 2002). The 4.8- $\mu\text{m}$  emission was noticeably subdued during the ‘fade’ of the SEB and the absence of convective activity at the time of the New Horizons encounter (2007) during a period of global upheaval (Rogers, 2008). However, the upheaval apparently had no effect on upper tropospheric temperatures or mid-IR aerosol opacity, implying that the effects of the upheaval were limited to the deeper cloud layers (e.g. below the 500-mbar level).
5. *Southern warm anomaly*: A region of enhanced temperatures extends southwest of the GRS in the 100–400 mbar range (the Southern Warm Anomaly, present throughout the 1995–2008 period) which has no counterpart in visible imaging or compositional/aerosol maps. The warm airmass extends into the South Temperate Belt and is sheared westwards by the retrograde jet at 28.7°S. However, the warm temperatures were perturbed by frequent encounters with cold airmasses associated with upwelling within Oval BA. No other perturbations to the internal thermal structure and composition of either vortex were observed during the interactions, but it is interesting to note that Oval BA began to exhibit its own southern warm anomaly after the reddening phase in 2005.
6. *Visibility of the peripheral ring*:  $\text{NH}_3$  within the GRS is not significantly enhanced over the surrounding atmosphere, but is usually separated by a region of depletion encircling the GRS. As with the ring of peripheral 4.8- $\mu\text{m}$  bright emission, this can appear as a complete ring or be completely absent. Both the  $\text{NH}_3$  depletion and the deep-cloud clearing are visible when upper tropospheric hazes within the GRS are clearly separated from the surroundings, but are absent or broken up when the haze appears more diffuse. Given the long-term stability of the GRS meteorology, the peripheral subsidence is likely to be a permanent feature of the atmospheric flow, albeit temporarily obscured from filtered imaging by overlying aerosols.
7. *Vertical temperature structure*: Finally, thermal wind calculations confirmed the despinning of anticyclonic motion of the GRS with altitude (Flasar et al., 1981), but also indicate that the thermal gradients in the GRS core and periphery move southward with increasing altitude. The north–south size (as measured in the CIRS and ground-based temperature retrievals and thermal winds, Fig. 5) appears larger at the tropopause than at 500 mbar by 1–2° latitude, whereas the east–west size is consistent for all altitudes.

It is hoped that the results derived in this study (the three-dimensional temperature structure, spatial distribution of atmospheric tracers and the temporal variability of these parameters)

will be used to refine models of the dynamics, chemistry and energetics of the GRS, as a paradigm for the formation of anticyclonic vortices on the giant planets. The correlations between visible and thermal data, particularly in the warm core of the vortex and in the peripheral ring of subsidence, suggest a chemical or dynamical link between the thermal environment and the red coloration of the GRS which should inform future models of chromophore production. The peripheral ring of subsidence effectively separates air within the GRS from air surrounding the vortex, and this long-term entrainment of material dredged from the deeper atmosphere (and subsequently photochemically processed) may be sufficient for the storm to maintain its red color.

From an observational standpoint, advances in our understanding of the GRS would be obtained by (a) full spectral modeling of the 1–5  $\mu\text{m}$  range concurrently with the thermal-IR to provide better constraints on particulate distributions within the GRS and other prominent jovian storms; (b) full spectral mapping capabilities between 5 and 25  $\mu\text{m}$  to improve on the filtered-imaging techniques used here; and (c) a continuous series of visible cloud-tracking measurements to monitor changes in the wind velocity at the same spatial resolution as the thermal and compositional maps. Finally, observations and modeling of the storm system in the radio (deep troposphere) and sub-mm (lower stratosphere) could reveal more about the vertical extent of the storm. One thing is clear: ground-based observations with 8.2-m telescopes and instrumentation in the thermal-IR will be an important complement to new results from the JUNO and Europa-Jupiter missions in the coming decades.

## Acknowledgments

Fletcher is supported by the Glasstone Science Fellowship at the University of Oxford, and both Fletcher and Parrish were supported during this research by appointments to the NASA Postdoctoral Program at the Jet Propulsion Laboratory, California Institute of Technology, administered by Oak Ridge Associated Universities through a contract with NASA. Orton and Yanamandra-Fisher carried out part of this research at the Jet Propulsion Laboratory, California Institute of Technology, under a contract with NASA. Orton acknowledges additional support from the Galileo and Cassini Projects. Irwin acknowledges the support of the UK Science and Technology Facilities Council. Edkins performed reduction of VLT/VISIR data while funded by the JPL Undergraduate Scholars (JPLUS) program. We thank the members of the Cassini/CIRS investigation team who have assisted in the design of the imaging sequences, instrument commands and other vital operational tasks, and the Ground Systems Operations for the Cassini Project. We also thank Rick Puetter for allowing us to use the PIXON image reconstruction algorithms. We recognize the hard work of Terry Martin, Leslie Tamppari, Larry Travis and Andy Lacy for making the Galileo/PPR observations possible. We wish to thank Robert Stencel (Denver University) for the loan of his 20.8- $\mu\text{m}$  filter, and two anonymous reviewers for their helpful suggestions.

We are grateful to the staff and telescope operators at the NASA/Infrared Telescope Facility (operated by the University of Hawaii under Cooperative Agreement No. NCC 5-538 with the National Aeronautics and Space Administration, Science Mission Directorate, Planetary Astronomy Program), the Subaru telescope (operated by the National Astronomical Observatory of Japan), the Gemini Observatory (operated by the Association of Universities for Research in Astronomy, Inc., under a cooperative agreement with the NSF on behalf of the Gemini partnership) and the ESO VLT (Paranal Observatories), without whom these studies (programme ID given in Table 1) could not have been undertaken. Fujiyoshi and Fuse were supported by the National Astronomical Observatory of Japan. Haywood was supported by the Gemini

Observatory, on behalf of the Gemini partnership: the National Science Foundation (United States), the Science and Technology Facilities Council (United Kingdom), the National Research Council (Canada), CONICYT (Chile), the Australian Research Council (Australia), Ministério da Ciência e Tecnologia (Brazil) and Ministerio de Ciencia, Tecnología e Innovación Productiva (Argentina).

## References

- Achterberg, R.K., Conrath, B.J., Gierasch, P.J., 2006. Cassini CIRS retrievals of ammonia in Jupiter's upper troposphere. *Icarus* 182, 169–180.
- Asay-Davis, X.S., Marcus, P.S., Wong, M.H., de Pater, I., 2009. Jupiter's shrinking Great Red Spot and steady Oval BA: Velocity measurements with the 'Advection Corrected Correlation Image Velocimetry' automated cloud tracking method. *Icarus* 203, 164–188.
- Baines, K., Carlson, R., Kamp, L., 2002. Fresh ammonia ice clouds in Jupiter. I. Spectroscopic identification, spatial distribution, and dynamical implications. *Icarus* 159 (1), 74–94.
- Baines, K.H., and 18 colleagues, 2007. Polar lightning and decadal-scale cloud variability on Jupiter. *Science* 318, 226–228.
- Banfield, D., Gierasch, P., Bell, M., Ustinov, E., Ingersoll, A., Vasavada, A., West, R., Belton, M., 1998. Jupiter's cloud structure from Galileo imaging data. *Icarus* 135 (1), 230–250.
- Beebe, R., 1994. Characteristic zonal winds and long-lived vortices in the atmospheres of the outer planets. *Chaos* 4, 113–122.
- Choi, D.S., Banfield, D., Gierasch, P., Showman, A.P., 2007. Velocity and vorticity measurements of Jupiter's Great Red Spot using automated cloud feature tracking. *Icarus* 188, 35–46.
- Conrath, B.J., Gierasch, P.J., Ustinov, E.A., 1998. Thermal structure and para hydrogen fraction on the outer planets from Voyager IRIS measurements. *Icarus* 135, 501–517.
- De Buizer, J., Fisher, R., 2005. TReCS and Michelle: The mid-infrared spectroscopic capabilities of the Gemini observatory. In: Käufel, H.U., Siebenmorgen, R., Moorwood, A. (Eds.), *High Resolution Infrared Spectroscopy in Astronomy*, Springer, pp. 84–87.
- Deutsch, L.K., Hora, J.L., Adams, J.D., Kassis, M., 2003. MIRS: A mid-infrared spectrometer and imager. In: Iye, Masanori, Moorwood, Alan, F.M. (Eds.), *Instrument Design and Performance for Optical/Infrared Ground-based Telescopes*. Proceedings of the SPIE, vol. 4841, pp. 106–116.
- Dowling, T.E., Ingersoll, A.P., 1989. Jupiter's Great Red Spot as a shallow water system. *J. Atmos. Sci.* 46, 3256–3278.
- Flasar, F.M., Conrath, B.J., Pirraglia, J., Clark, P.C., French, R.G., Gierasch, P.J., 1981. Thermal structure and dynamics of the jovian atmosphere. I – The Great Red Spot. *J. Geophys. Res.* 86, 8759–8767.
- Flasar, F.M., and 44 colleagues, 2004. Exploring the Saturn system in the thermal infrared: The composite infrared spectrometer. *Space Sci. Rev.* 115, 169–297.
- Fletcher, L.N., Orton, G.S., Teanby, N.A., Irwin, P.G.J., 2009a. Phosphine on Jupiter and Saturn from Cassini/CIRS. *Icarus* 202, 543–564.
- Fletcher, L.N., Orton, G.S., Yanamandra-Fisher, P., Fisher, B.M., Parrish, P.D., Irwin, P.G.J., 2009b. Retrievals of atmospheric variables on the gas giants from ground-based mid-infrared imaging. *Icarus* 200, 154–175.
- García-Melendo, E., Legarreta, J., Sánchez-Lavega, A., Hueso, R., Pérez-Hoyos, S., González, J., Gómez-Forrellad, J.M., the IOPW Team, 2009. The jovian anticyclone BA. I. Motions and interaction with the GRS from observations and non-linear simulations. *Icarus* 203, 486–498.
- Go, C., and 10 colleagues, 2008. Jupiter's south equatorial belt outbreak spots and the SEB fade and revival cycle. In: *Bulletin of the American Astronomical Society*, vol. 40. Bulletin of the American Astronomical Society, p. 475.
- Griffith, C., Bézard, B., Owen, T., Gautier, D., 1992. The tropospheric abundances of NH<sub>3</sub> and PH<sub>3</sub> in Jupiter's Great Red Spot, from Voyager IRIS observations. *Icarus* 98 (1), 82–93.
- Hanel, R., Conrath, B., Kunde, V., Lowman, P., Maguire, W., Pearl, J., Pirraglia, J., Gautier, D., Gierasch, P., Kumar, S., 1977. The Voyager infrared spectroscopy and radiometry investigation. *Space Sci. Rev.* 21, 129–157.
- Hanel, R., and 12 colleagues, 1979. Infrared observations of the jovian system from Voyager 1. *Science* 204, 972–976.
- Hanel, R.A., Conrath, B.J., Jennings, D.E., Samuelson, R.E., 2003. Exploration of the Solar System by infrared remote sensing. In: Hanel, R.A., Conrath, B.J., Jennings, D.E., Samuelson, R.E. (Eds.), *Exploration of the Solar System by Infrared Remote Sensing*, second ed. Cambridge University Press, Cambridge, UK. ISBN: 0521818974.
- Irwin, P.G.J., Parrish, P., Fouchet, T., Calcutt, S.B., Taylor, F.W., Simon-Miller, A.A., Nixon, C.A., 2004. Retrievals of jovian tropospheric phosphine from Cassini/CIRS. *Icarus* 172, 37–49.
- Irwin, P., Teanby, N., de Kok, R., Fletcher, L., Howett, C., Tsang, C., Wilson, C., Calcutt, S., Nixon, C., Parrish, P., 2008. The NEMESIS planetary atmosphere radiative transfer and retrieval tool. *J. Quant. Spectrosc. Radiat. Trans.* 109 (6), 1136–1150.
- Kataza, H., Okamoto, Y., Takubo, S., Onaka, T., Sako, S., Nakamura, K., Miyata, T., Yamashita, T., 2000. COMICS: The cooled mid-infrared camera and spectrometer for the Subaru telescope. In: Iye, M., Moorwood, A.F. (Eds.), *Society of Photo-Optical Instrumentation Engineers (SPIE) Conference Series*, vol. 4008. Presented at Society of Photo-Optical Instrumentation Engineers (SPIE) Conference, pp. 1144–1152.
- Lara, L., Bézard, B., Griffith, C., Lacy, J., Owen, T., 1998. High-resolution 10-micrometer spectroscopy of ammonia and phosphine lines on Jupiter. *Icarus* 131 (2), 317–333.
- Limaye, S.S., 1986. Jupiter – New estimates of the mean zonal flow at the cloud level. *Icarus* 65, 335–352.
- Matcheva, K., Conrath, B., Gierasch, P., Flasar, F., 2005. The cloud structure of the jovian atmosphere as seen by the Cassini/CIRS experiment. *Icarus* 179 (2), 432–448.
- Mitchell, J.L., Beebe, R.F., Ingersoll, A.P., Garneau, G.W., 1981. Flow fields within Jupiter's Great Red Spot and White Oval BC. *J. Geophys. Res.* 86, 8751–8757.
- Orton, G.S., Spencer, J.R., Travis, L.D., Martin, T.Z., Tamppari, L.K., 1996. Galileo photopolarimeter–radiometer observations of Jupiter and the Galilean satellites. *Science* 274, 389–391.
- Porco, C.C., and 23 colleagues, 2003. Cassini imaging of Jupiter's atmosphere, satellites, and rings. *Science* 299, 1541–1547.
- Puetter, R.C., Yahlil, A., 1999. The Pixon method of image reconstruction. In: Mehringer, D.M., Plante, R.L., Roberts, D.A. (Eds.), *ASP Conference Series 172: Astronomical Data Analysis Software and Systems VIII*, pp. 308–316.
- Read, P., Gierasch, P., Conrath, B., 2006. Mapping potential-vorticity dynamics on Jupiter. II: The Great Red Spot from Voyager 1 and 2 data. *Quart. J. R. Meteorol. Soc.* 132 (618), 1605–1625.
- Ressler, M., Werner, M., Cleve, J., Chou, H., 1994. The JPL deep-well mid-infrared array camera. *Exp. Astron.* 3 (1), 277–280.
- Reuter, D.C., and 10 colleagues, 2007. Jupiter cloud composition, stratification, convection, and wave motion: A view from new horizons. *Science* 318, 223–225.
- Rio, Y., Lagage, P.O., Dubreuil, D., Durand, G.A., Lyraud, C., Pel, J.-W., de Haas, J.C., Schoenmaker, A., Tolsma, H., 1998. VISIR: The mid-infrared imager and spectrometer for the VLT. In: Fowler, A.M. (Ed.), *Proceedings of the SPIE*, vol. 3354, pp. 615–626.
- Rogers, J., 1995. *The Giant Planet Jupiter*. Cambridge University Press.
- Rogers, J.H., 2008. Progress of Jupiter's global upheaval. *J. Brit. Astron. Assoc.* 118, 9.
- Russell, E.E., Brown, F.G., Chandos, R.A., Fincher, W.C., Kubel, L.F., Lacinis, A.A., Travis, L.D., 1992. Galileo photopolarimeter/radiometer experiment. *Space Sci. Rev.* 60, 531–563.
- Sada, P.V., Beebe, R.F., Conrath, B.J., 1996. Comparison of the structure and dynamics of Jupiter's Great Red Spot between the Voyager 1 and 2 encounters. *Icarus* 119, 311–335.
- Sánchez-Lavega, A., and 12 colleagues, 2001. The merger of two giant anticyclones in the atmosphere of Jupiter. *Icarus* 149, 491–495.
- Simon-Miller, A.A., Banfield, D., Gierasch, P.J., 2001. Color and the vertical structure in Jupiter's Belts, zones, and weather systems. *Icarus* 154, 459–474.
- Simon-Miller, A., Gierasch, P., Beebe, R., Conrath, B., Flasar, F., Achterberg, R., 2002. New observational results concerning Jupiter's Great Red Spot. *Icarus* 158 (1), 249–266.
- Simon-Miller, A.A., Conrath, B.J., Gierasch, P.J., Orton, G.S., Achterberg, R.K., Flasar, F.M., Fisher, B.M., 2006. Jupiter's atmospheric temperatures: From Voyager IRIS to Cassini CIRS. *Icarus* 180, 98–112.
- Smith, B.A., and 22 colleagues, 1979. The Jupiter system through the eyes of Voyager 1. *Science* 204, 951–957.
- Terrile, R.J., Capps, R.W., Backman, D.E., Becklin, E.E., Brown, R.H., Cruikshank, D.P., Beichman, C.A., Westphal, J.A., 1979. Infrared images of Jupiter at 5-micrometer wavelength during the Voyager 1 encounter. *Science* 204, 1007–1008.
- Vasavada, A.R., Showman, A.P., 2005. Jovian atmospheric dynamics: An update after Galileo and Cassini. *Rep. Prog. Phys.* 68, 1935–1996.
- Vasavada, A.R., and 13 colleagues, 1998. Galileo imaging of Jupiter's atmosphere: The Great Red Spot, equatorial region, and white ovals. *Icarus* 135, 265–275.
- Wong, M.H., Bjoraker, G.L., Smith, M.D., Flasar, F.M., Nixon, C.A., 2004. Identification of the 10- $\mu$ m ammonia ice feature on Jupiter. *Planet. Space Sci.* 52, 385–395.